

R-957
CU-314
NEVIS-208

Nevis Laboratories
Columbia University
Physics Department
Irvington-on-Hudson
New York

The Observation of Directly Produced Electrons
and Positrons in Hadron-Hadron Collisions

HANS P. PAAR

Reproduction in whole or in part
is permitted for any purpose of the
United States Government

Submitted in partial fulfillment of
the requirements for the degree
of Doctor of Philosophy in the Faculty
of Pure Science, Columbia University

1975

National Science Foundation
GP 33435

The Observation of Directly Produced Electrons
and Positrons in Hadron-Hadron Collisions^{*}

HANS P. PAAR[†]

Columbia University, New York, N.Y.

* Research supported by the National Science Foundation.

† Submitted in partial fulfillment of the requirements for the degree of Doctor of Philosophy in the Faculty of Pure Science.

ABSTRACT

Directly produced electrons have been observed in $p\text{Be} \rightarrow e^\pm X$ with 300 GeV/c incident protons. The invariant cross section for this process is given at 65° and 93° in the proton-nucleon center of mass (50 and 83 mr in the laboratory) as a function of the transverse momentum P_T of the electron. The cross section falls 4 decades for P_T in the range 1.8 to 4.0 GeV/c. There is no evidence for bumps in the transverse momentum spectrum. The ratio of electrons to π^0 's is $(0.8 \pm 0.1) \times 10^{-4}$ at 90° c.m. and $(1.6 \pm 0.2) \times 10^{-4}$ at 65° c.m. The charge asymmetry $(e^+ - e^-)/(e^+ + e^-) = (0.040 \pm 0.075)$ at 65° and (0.14 ± 0.09) at 93° independent of P_T . The possible origin of the electrons is discussed and a comparison is made with a parton model prediction. There is no evidence of heavy particles such as the intermediate vector boson W^\pm in the mass range 5.0 to 11 GeV/c².

TABLE OF CONTENTS

	<u>Page</u>
I. Introduction	1
II. Apparatus	6
A. General Requirements	6
B. Electrons versus Muons	6
C. General Layout	7
D. Apparatus Details	8
III. Data Acquisition	14
A. Triggering Considerations	14
B. DC Logic	15
C. Data Recording and Operation	16
IV. Data Analysis and Results	18
A. Standard Data Analysis	18
B. Results	25
C. Studies	28
V. Interpretation of Results and Conclusions	34
A. Summary of Results	34
B. Sources of Leptons	35
C. Known Sources: Vector Mesons, η 's, Virtual Photons	36
D. Intermediate Bosons	37
E. Anomalous Interactions	38
Acknowledgments	39
Appendices	40
References	62
Tables	68
Figures	77

I. INTRODUCTION

The observation of directly produced leptons in hadron-hadron collisions is of interest for two reasons. First, it allows us to probe the structure of hadrons much in the same way as deep inelastic electron nucleon scattering does, see Figs. 1 and 2.

In both cases, the vertex at the lepton end of the virtual photon is given by quantum electrodynamics. What happens at the other end depends upon the particular model that one assumes for the nucleon. The observation of leptons could distinguish between different models and so in this sense one measures the structure of the nucleon. Second, the production of exotic particles such as the intermediate vector boson W^\pm , the Lee-Wick boson B^0 , Weinberg's Z and ϕ , heavy leptons or charmed particles could give rise to leptons through their leptonic decay modes. The observation of these leptons can give information about these structures. In the past, these considerations have motivated much work.

In the late 1930's, the measurement of the magnetic moment of the proton and later the neutron gave the first indication of a possible structure within the hadron. The work by Rabi and collaborators and others using molecular beams gave a value for these magnetic moments very different from what one would expect if the proton and neutron were elementary particles with electromagnetic structure only. The discovery of the pion led to the introduction of the

concept of a pion cloud around the nucleon very much like the virtual photon cloud around the electron. This allows a qualitative explanation of the nucleon's anomalous magnetic moment. The introduction of two form factors F_1 and F_2 to describe the electromagnetic current of hadrons in elastic electron hadron scattering and their measurement in the 1950's by Hofstadter and collaborators led to a phenomenological description of the distribution of charge and magnetic moment in the proton and neutron. In this work, electrons were scattered off nuclei, a process described in lowest order by the exchange of a virtual photon. The form factors are functions of q^2 only (q_μ is the photon's four-momentum) if one ignores the production of pions and of excited states in the target nucleus.

In the 1960's, these measurements were extended to deep inelastic electron nucleon scattering in which the target nucleon is broken up. The process is described by the graph of Fig. 2. Two form factors W_1 and W_2 are introduced which are now functions of q^2 and the energy transfer ν to the initial hadron, see Fig. 2. At the end of the 1960's, attempts were made to explain the experimental results in terms of particular models of constituents within the nucleon. The best known among these is Feynman's parton model. This model led to Bjorken's scaling prediction which says that the just mentioned form factors W_1 and W_2 are not

functions of q^2 and ν individually but rather are a function of q^2/ν in the appropriate kinematic region.

The scaling prediction has been verified experimentally. In all these processes, the exchange of a spacelike virtual photon takes place. It is of interest to extend this to the timelike region. The experiment by Christenson et al¹ observed a pair of muons produced in hadron-hadron collisions by a timelike photon, Fig. 1.

Again, there are various models to describe the production of the photon from the hadron-hadron collision. For example, in the parton model, a favored mechanism is the annihilation of a parton and an antiparton into the virtual photon.² In this model, a scaling prediction results also. This scaling prediction has not been verified yet. The above-mentioned search for the intermediate vector boson W is motivated by ideas developed in the 1930's.

In 1934, one year after Fermi published his theory of the β decay of the nucleus, Yukawa speculated that this interaction could be mediated by a particle.³ This particle is conventionally called W boson. By now, various authors have postulated a variety of W bosons: charged and neutral, spin 0 and 1, strongly and not strongly interacting.⁴ Many searches have been made;⁵ it has not been detected. This means that if the W exists, its mass M_W must be greater than $10.3 \text{ GeV}/c^2$.⁶ The W boson could decay weakly into a charged

lepton and its neutrino with a lifetime of order $G^2 M_W^3 < 10^{-17}$ sec where G is the universal Fermi coupling constant. Consequently, the lepton will be produced extremely close to the origin of the W boson. A clear signature of the W is a bump in a plot of the lepton production cross section vs its transverse momentum P_T at $P_T = M_W/2$, if the W is produced with negligible transverse momentum.⁷ The discussion of the detection of the W boson can be applied to the other particles above.

The B^0 particle is introduced to mediate the electromagnetic interaction (heavy photon) and to make the subtraction in the renormalization program of quantum electrodynamics finite.⁸

More recently, a gauge theory of weak and electromagnetic interactions of leptons has been introduced.^{9,10,11} This theory is renormalizable thereby allowing the calculation of higher order weak processes. In order to obtain finite results, in processes involving leptons, new particles are introduced leading to additional graphs whose divergences cancel the original divergences that are encountered. The theory must have either neutral currents Z_μ (the Weinberg-Salam version⁹) or heavy leptons M (the Georgi-Glashow version¹⁰) or both.¹¹ All have spin 0 Higg's bosons. Through the decay modes $Z \rightarrow l^+ l^-$ and $M \rightarrow l \nu_l \nu_M$, these new objects could give rise to leptons. There is evidence of

neutral currents¹² but not of heavy leptons. A limit of $M_{M^+} \geq 8.4 \text{ GeV}/c^2$ exists for the mass of a muonlike heavy lepton,⁶ if its branching ratio into leptons is larger than 0.3. The introduction of hadrons into the gauge theory leads to new divergences. These cannot be remedied by the introduction of new particles because a $\Delta S = 1, \Delta Q = 0$ current is not observed experimentally ($K^+ \rightarrow \pi^+ \nu \bar{\nu}$ and $K^+ \rightarrow \pi^+ e^+ e^-$ are suppressed strongly). One way out is to introduce a new quantum number (called charm).¹³ It is assumed that C is conserved in strong and electromagnetic interactions and that all known stable hadrons have $C = 0$. A charmed particle produced in a hadron-hadron collision can decay like $C \rightarrow \text{hadron} + \text{lepton} + \text{neutrino}$ and give rise to leptons. In 3-body decays, such as the heavy lepton and charmed particles, a peak in the transverse momentum spectrum would appear but this peak would be wider than a peak from 2-body decays such as the W above.

An abundant production of vector mesons V such as $\rho, \omega,$ and ϕ can give rise to a much larger lepton yield than the sources mentioned above through their decay, $V \rightarrow l^+ l^-$. The production cross section for these at large P_T is not known and consequently the lepton yield due to these sources is unknown. Estimates are given in Sec. V where it is shown how the vector mesons affect the sensitivity of the experiment to the more interesting new particles, W, Z, M, C, etc. mentioned earlier.

II. APPARATUS

A. General Requirements

From Sec. I, it follows that we want to detect a continuous spectrum of leptons with possible bumps superposed on it.

To do this, one needs a good momentum or energy resolution and it is helpful to have a continuous momentum acceptance over a wide range of momenta for a given setting of the spectrometer. In addition, the cross section for hadron production is much larger than for lepton production (about 10^4). It is therefore necessary to have an excellent hadron rejection ($\gg 10^4$) with good efficiency for leptons in order to be able to detect the leptons in this large hadronic background. A third requirement is that the detectors must have a good rate capability in order to function properly in the large flux of hadrons coming from the target.

B. Electrons versus Muons

A better resolution can be obtained by detecting electrons rather than muons in the final state. The reason for this is the different manner in which one accomplishes the required large hadron-rejection mentioned in A.

If one detects muons in the final state, it is necessary to place a hadron absorber near the target to absorb hadrons, especially pions and kaons which give rise to muons through their muon decay modes. The resulting multiple scattering makes the momentum resolution (roughly 3 x) worse than in the

case where electrons are detected in the final state. In this case, there is of course no absorber but electron hadron discrimination can be obtained through the use of a lead glass total absorption calorimeter in a way explained below. It depends upon the fact that hadron and electron induced showers in this calorimeter are very different in character and that electrons always deposit all their energy while hadrons very rarely do. The production in the target of a large flux of high energy photons from π^0 and η^0 decays gives rise to electrons through the conversion of the photons in the target and miscellaneous matter that is distributed along the path from target to detector. These sources of electrons must be understood and subtracted.

C. General Layout

In the experiment, the extracted proton beam of the Fermilab strikes a thin target. The apparatus then detects charged particles (and indirectly photons) originating at the target. It consists of i) a collimator which selects the angle in the laboratory, ii) two bending magnets to select charged particles of one sign and to measure their momentum, iii) a series of hodoscopes to define a particle's trajectory from the target through the magnet to the end of the spectrometer, iv) a lead glass total absorption calorimeter to measure the energy of electrons and to obtain hadron rejection and lastly, v) a hadron calorimeter to monitor hadronic showers allowing muon-hadron discrimination.

D. Apparatus Details

We will now discuss the various components of the apparatus, in more detail, going from upstream to downstream.

The extracted proton beam of the Fermilab accelerator strikes a beryllium target located in the proton laboratory. Its intensity is monitored continuously by a secondary emission monitor (SEM). Beryllium is chosen because a low Z material is needed in order to reduce photon conversions in the target. The target is 10.26 cm long. The inelastic nucleon interaction length of beryllium is 39.5 cm,¹⁴ so this corresponds to 26% of an inelastic interaction length. The beam is brought to a $0.4 \times 3 \text{ mm}^2$ focus which results in 60% targeting efficiency. Because the production angle θ_{LAB} is chosen in the horizontal plane, the target is thin in that direction (0.224 mm) so secondaries leave the target at the side. The end effect of the length of the target can be ignored. Using 35.7 cm for the radiation length of beryllium, this means that secondaries traverse on the average 0.92% of a radiation length at $\theta_{\text{LAB}} = 50 \text{ mr}$ and 0.60% at $\theta_{\text{LAB}} = 83 \text{ mr}$. Vertically, the target is larger than the beam. After traversing the target, the residual protons and forward produced secondaries are totally absorbed in a dense beam dump, located 2.2 m downstream from the

target. The target and beam dump are shielded by a target box with helium gas in it to reduce the amount of radiation length in the path of the secondaries. The purity of this gas is monitored during the experiment. The air contamination was always less than 0.2% which corresponds to an additional 0.005% of a radiation length. The number of interactions in the target is monitored by a target monitor called QED. This monitor views the target at 116 mr. It is a triple coincidence between a lucite Cerenkov counter (Q) and two scintillation counters (D and E). Its response to the flux of muons emerging from the beam dump is $< 0.5\%$. The production angle θ_{LAB} chosen in the horizontal plane by positioning a steel collimator at the required angle. Its angular acceptance is 9 mr x 9 mr. At the front end the walls are lined with a tungsten alloy. The collimator is followed by 2 bending magnets which bend in the vertical direction. The collimator and the first magnet are evacuated. A path in helium gas is created through the second magnet up to the first hodoscope. After allowing for sufficient drift space to accomplish a spatial separation between charged and neutral particles, there follows a set of hodoscopes ($H_1, U, V, V_1, M, H_2, V_2$) and trigger counters (T_O, T_M, T_1). The hodoscopes consist of 210 elements: horizontal and vertical strips of scintillator each of which has a photomultiplier on it. The strips are overlapping

as shown in Fig. 26. Horizontal strips 1.905 cm wide (H_1 and H_2 hodoscopes) measure the vertical deflection of the particle and therefore its momentum. The resolution σ_p (standard deviation) is given by $\sigma_p/P = 0.18 P/I$ where P is the particle's momentum in GeV/c and I the current in the magnet in amperes, see Appendix I. Typical values are $P = 30$ GeV/c, $I = 500$, so $\sigma_p/p = 1\%$. This is a lower limit because the inefficiency of the hodoscopes is ignored. Vertical strips 1.905 cm wide (V_1 and V_2 hodoscopes) measure the production angle at the target with a resolution of 0.2 mr.

The U (strips 7.62 cm wide at 45°) and M (horizontal strips 7.62 cm wide) hodoscopes are for ambiguity resolution to be discussed below. Then follows a lead glass calorimeter and a hadron calorimeter. Leadglass is glass with lead oxide added to get a short radiation length. The lead concentration must be limited in order that the glass remains sufficiently transparent for Cerenkov light. Table I gives the properties of the glass used in the experiment.

An electron will give rise to an electromagnetic shower in the lead glass. The depth is chosen such that more than 99% of the shower energy is contained. The electrons in the shower will give Cerenkov light if their velocity $\beta > 1/n$ or $E > 0.92$ MeV where n is the refraction

index of the lead glass. The lead glass array consists of 45 blocks of lead glass (each 15 x 15 x 35 cm). The light is detected by 45 photomultipliers. The blocks are arranged as shown in Fig. 4. Some details of the operation of the lead glass are given in Appendix II and Ref. 15. It is shown there that under certain conditions, the area of the photomultiplier output pulse is proportional to the energy of the incident electron. The determination of the proportionality constant and its variation with time is the subject of Appendix III. The lead glass calorimeter is divided in 3 layers, see Fig. 4. Each block is optically insulated from the others. This allows one to monitor the shower development and thereby improve hadron rejection. The lead glass array is 1.3 absorption lengths deep. So on the average, hadrons deposit only a small fraction of their energy in the glass. Due to large fluctuations in the hadronic shower development and charge exchange reactions (e.g. $\pi + n \rightarrow p\pi^0$), some hadrons (few times, 10^{-4}) deposit more than 95% of their energy. In general, the hadron induced shower will develop in a different way.

Downstream of the first layer, a set of trigger counters called T_2 gives information about the early start of the shower. Clearly the requirement that an electromagnetic shower begins after a few radiation lengths of matter that introduces a minimal amount of nuclear interaction length in the beam will improve hadron rejection still further.

The sheet of lead sandwiched between E_p and E counters upstream of the lead glass calorimeter allows for this (2.3 radiation lengths and 0.18 nuclear interaction lengths). A pulse height corresponding to a few minimum ionizing particles can be required in counter E . This requirement tends to select electrons but also hadrons which interacted in matter upstream of the E counter (lead sheet, hodoscopes, air). To minimize this effect, one requires no more than one minimum ionizing particle in the E_p counter just upstream of the lead sheet.

The lead glass calorimeter is followed by 10 cm of lead (0.52 absorption lengths) to further absorb the very soft shower products that emerge from the lead glass array. This is followed by 4 layers of scintillation counters called πe . Between layers of scintillator there are 1.3 cm thick aluminum sheets to range out soft particles that could be produced in the scintillator upstream. These counters give hadron rejection by requiring that no more than 2 along a track register a particle. A hadron will in general register 4 along a track because even when a hadron deposits nearly all its energy in the lead glass array, some hadrons can emerge from it. The hadron calorimeter¹⁶ consists of 88 cm of steel (4.4 absorption lengths) interspersed with 4 scintillation counters, called $\pi\mu$. These counters pulse area is registered. The development of a hadronic shower will give large pulse heights. If all 4 register a minimum

ionizing particle, we have a muon (or a non-interacting hadron).

The last element of the detector is a 16 element hodoscope with vertical strips of scintillator 5.1 cm wide. They give additional muon-hadron discrimination. For a muon only one strip should register a particle. The one that fires has to be consistent with the track information of the hodoscopes and the amount of multiple scattering expected in the steel of the hadron calorimeter and the lead glass.

The dimensions and location of the various elements of the spectrometer lead to a wide momentum acceptance, see Fig. 5 and Appendix IV for calculations. With 2 or 3 magnet current settings, a wide range of transverse momenta can be covered with good acceptance and considerable overlap between them allowing for consistency checks. During a running cycle, we introduced in turn a series of thin brass converters into the flux of particles from the target. The thicknesses correspond to 2, 4, and 6% of a radiation length. This allows one to extrapolate the electron yield to zero matter, the resulting yield corresponds to directly produced electrons.

One obtains by this procedure, the photon spectrum as well and from this the π^0 spectrum if one assumes that all photons were produced by π^0 decay. In addition to running, with the 3 converters and no converter at all, runs were

taken with a 5.1 cm thick lead filter. This removes all electrons from the beam (actually the intense flux of photons produces a negligible yield of electrons, see Appendix V).

Events which then still satisfy the electron criteria are surely hadrons and should therefore be subtracted. The procedure is described in Sec. IV. Using this the hadron rejection is $> 10^5$.

III. DATA ACQUISITION

A. Triggering Considerations

The electron trigger must have enough hadron rejection to reduce the trigger rate to a level that is acceptable with respect to deadtime yet it must have high efficiency for electrons.

Because there are 10^4 hadrons for every electron, the trigger necessarily had to include some information about the shower in the lead glass calorimeter. This information is supplied by the pulse height from T_2 and by the summed pulse height E_{12} from the dynodes of the 20 photomultipliers of the first and second layer of lead glass. The choice of these 20 is the result of a compromise between having available information about the total energy deposited in the lead glass calorimeter and an early shower development.

The pulse height from the lead glass calorimeter is discriminated at 3 different levels called E_{12L} , E_{12M} , and E_{12H} , see Fig. 6. The E_{12L} level is low enough so that

all electrons have their pulse height larger than E12L. Typical values for these levels are 12, 25 and 31 GeV at $\theta_{\text{LAB}} = 83$ mr. The triggers derived from the lowest two thresholds are prescaled in order to get roughly equal trigger rates for all three. Prescaling allows one to reduce the trigger rate at will by triggering only on every 2nd or 4th or 8th etc. threshold crossing of E12L and E12M. The information from the hodoscopes is stored in a set of coincidence registers (CR's), one for each element. The CR's make available information about how many elements per plane had a count. This information is used in the trigger as well. All 3 electron triggers require at least 1 count per plane. Table II gives a table with typical trigger rates for a run with no converter and a run with 5.1 cm lead filter.

B. DC Logic

Because of the sophistication of this decision making this part of the logic operates with about 120 ns deadtime. It is called DC logic. Because of this deadtime, the DC logic should not be triggered more than a few times 10^5 /sec. The trigger for the DC logic is supplied by the fast logic. A triple coincidence between $T_0 T_M T_1$ is prescaled and allows triggering on any charged particle (mostly hadrons). A coincidence between the unprescaled $T_0 T_M T_1$ and T_2 greatly enriches the trigger with electron type events where a shower was started (either

electromagnetic or hadronic) in the first layer of lead glass.

T_2 reduces the $T_O T_M T_1$ rate by a factor 20 to 40, low enough to trigger the DC logic. There are 5 standard triggers derived from the DC logic: 3 electron triggers (fast logic trigger $T_O T_M T_1 T_2$) with at least 1 count in each hodoscope, no more than 2 πe firing along a track and pulseheight E12 large enough to cross E12L, M or H, respectively: The fourth a hadron trigger (fast logic trigger $T_O T_M T_1$ prescaled) and at least 1 count in each hodoscope plane. The fifth one a random trigger derived from the QED target monitor. This trigger allowed us to study pileup effects in the lead glass calorimeter as well as other intensity dependent effects such as reconstruction efficiency, see Sec. IV.

C. Data Recording and Operation

Any one of these 5 triggers started the pulse height analysis of 59 photomultipliers, 45 for the lead glass calorimeter, 4 for the $\pi\mu$, 4 for T_2 , 3 for E and 3 for EP. This takes about 10 μs , then a trigger is sent to the PDP 15 on line computer which reads and stores the pulseheights and hodoscope information and a 16 bit logic word (describing the status of the slow logic) in a buffer.

At the end of the spill of the accelerator, the contents of scalers are stored in the buffer. When the

buffer is full or when the spill of the machine ends, the contents of this buffer are written on magnetic tape for data off line analysis.

During the run, an on line program monitors the performance of the detectors and analyzes a fraction of the events. At the end of a run, this information is printed out in the form of tables and histograms together with contents of scalers.

A running period is divided into cycles, each cycle consists of 10 runs with different converters, no converter or with the lead filter. For these runs, the 5 standard data triggers are used. Two runs in each cycle were study runs to check on the efficiencies of the electron trigger, see Sec. IV. At the end of each cycle, the current in the magnet and/or its polarity was changed to reduce systematic effects.

Every 24 to 48 hours, the lead glass calorimeter was calibrated with muons as described in Appendix III. The trigger for these runs was $T_O T_M T_1$ with 1 or 2 counts per hodoscope plane and a single count in the "mu-picket" hodoscope situated behind the hadron calorimeter.

IV. DATA ANALYSIS AND RESULTS

This section is divided into three parts: A. The standard data analysis, B. Results, and C. Studies which attempt to justify the procedures that are employed. This order is chosen to accommodate the reader who is mainly interested in the results. Others may start with part C and then A and B.

A. Standard Data Analysis

1. Introduction

The off line analysis starts with the information written on magnetic tape during the running. Its result is the invariant cross section $E \frac{d^3\sigma}{dp^3}$ as a function of P_T with special emphasis on the presence of possible bumps and charge asymmetry defined as $(e^+ - e^-)/(e^+ + e^-)$. A good hadron rejection must be obtained which necessitates tight cuts on the data and a subtraction of background (measured by the lead filter runs). Therefore a determination of cut efficiency and of possible biases caused by either cuts or the trigger has to be made.

The main parts of the analysis are:

1. reconstruction of events using only the hodoscope information,
2. cuts on data using the pulse height information and the results of 1,
3. extrapolation to zero matter in the beam of secondaries,
4. subtraction of hadrons that pass the electron cuts.

2. Track Reconstruction

The reconstruction efficiency is 80 to 90% for the electron trigger; it depends upon the intensity of the incident beam.

The most important effects that cause the loss of 10 to 20% are given in Table III. The triggering efficiency of the hodoscopes is discussed in Sec. IV.C. Once it has been verified that the track originates from the target in the horizontal plane, it is necessary to assume that the track originated from the target in the vertical plane in order to calculate the momentum p . This assumption can be tested for electrons because p and E must be the same within an accuracy given by the resolutions. The result of a successful reconstruction is the momentum and position of the particle everywhere in the spectrometer. To calculate the momentum, a map of $\int B d\ell$ of each magnet was used.

3. Geometric Cuts

Using this information, the following fiducial cuts are applied. At the target: i) the angle of the track with the axis of the collimator must be less than 4.2 mr in the horizontal and vertical plane; ii) at the exit face of the second magnet, the track should vertically be no more than 12.7 cm from the axis of the magnet; iii) the track should be no closer than 7 cm from the edge of the lead glass calorimeter.

4. Shower Development Cuts

For the events that reconstruct it is known which blocks of the lead glass calorimeter participate in the shower. (The transverse dimension of the shower is discussed in Sec. IV.C.) We sum only the pulse heights of these blocks in order not to overestimate the electron's energy due to pileup effects (discussed in Sec. IV.C). If a particle enters near a crack between 2 blocks, an experimentally determined correction is made to account for the resulting smaller energy deposition. A transit correction (typically 5%) is made for the blocks in the first and second layer. This corrects for attenuation of the Cerenkov light in reaching the photomultiplier. Events with $E_1 + E_2 < E_c$ with E_c chosen to be higher than the $E_{12}L$ threshold are cut. E_1 is the energy deposited in the first layer of glass etc. This cut eliminates the effects of drifts in the $E_{12}L$ threshold. The electron trigger required that fewer than four πe fire along a track. About 10% of the electron triggers have 3 πe firing along a track; these are hadrons and are cut. See also Sec. II for a definition of πe and Sec. IV.C. for a discussion.

5. Electron Identification

At this point the analysis proceeds two different ways according to what cuts are used to reduce hadrons. This allows us to check the internal consistency of the analysis.

Type 1 Cut: Shower development cuts.

The difference in shower development of hadronic and electromagnetic showers in the lead glass calorimeter is exploited. E_1/E , E_2/E and E_3/E are required to be within an interval whose bounds are slightly momentum dependent. The bounds are determined such that hadron rejection is almost independent of momentum using guaranteed electron induced and hadron induced showers as described in Sec. IV.C.

Type 2 Cut: E and EP counter cuts.

This cut requires the shower to start in the lead sheet between the EP and E counters. We required more than 3 times minimum ionizing pulse height in E and less than 2 in EP. Thus, this demands a single incoming track and a rapid buildup of a shower in 2.3 radiation lengths and 0.18 of a nuclear interaction length, see Sec. II.

The effects of these cuts can be seen in Figs. 7 and 8. A histogram of E/P is given. Hadrons deposit an amount of energy in the lead glass less than or equal to P . Electrons deposit all their energy so $E \approx P$ within a few percent due to the resolution in E and P . The peak near $E/P \approx 1$ is due to electrons, the continuum under it and at lower E/P values due to hadrons. The type 1 and type 2 cuts reduce the hadronic background considerably. This can be seen from Table II. The hadrons that pass all electron cuts must be removed by

subtraction. The runs with the 5.1 cm lead filter are used for this. If one compares E/P distributions of runs with different converters, no converter and the lead filter and normalizes to the number of events in the region $0.76 \leq E/P \leq 0.87$ (a region without electrons) the E/P distribution can be seen to overlap perfectly outside the electron peak. It is assumed that the shape of the hadronic background under the electron peak is correctly given by the shape of the lead filter runs. This assumption is crucial. Normalizing as described, this residual hadronic background can be subtracted.

6. Prescalar Treatment

The E12L and E12M triggers were prescaled in order to limit the number of events with low energy. These are relatively abundant because of the steeply falling spectrum. The events which were triggered by E12L only are used for studies for example to determine the efficiency of E12M. In order to recover the original spectrum, we apply a weight to each event according to which E12 level triggered (as can be determined from the logic word, III.C.). If it was triggered by E12H (irrespective of E12M) the weight is 1. If it was triggered by E12M and not E12H, the weight is equal to the prescaling factor.

The prescaling factor set by an electronic circuit was measured experimentally by determining what fraction of

events triggered by E12H were also at the same time triggered by E12M. The inverse of the prescaling factor should be equal to this fraction. It was always within 5%.

7. Extrapolation to Zero Matter; Converter Curve

We present the data in the following way. In the E/P histogram, we define two intervals, ($0.76 \leq E/P \leq 0.87$) one which contains only hadrons (total number of events h') and one which contains the electron peak ($0.93 \leq E/P \leq 1.07$) plus hadronic background under it (e'). The ratio e'/h' is a quantity which only depends upon the converter for a given angle in the lab and a given magnet current. The ratio is plotted in Fig. 9 for a typical cycle. The data points are averages of several runs. Their internal consistency is excellent. The data points are corrected for bremsstrahlung losses of the electrons.

One might think that this is a negligible effect because we have thin radiators ($< 8\%$ of a radiation length). However, because of the steeply falling spectrum of electrons and photons, even a small energy loss leads to a relatively large change in rate.

In order to produce an electron with a given energy, one must start with an electron or photon with a somewhat higher energy whose yield is lower leading to corrections of order of 2 to 15% depending upon the converter thickness.²⁹

After this correction, the data points are seen to lie on a straight line. A fit gives a χ^2 of 0.14 for 2 degrees of freedom. The e'/h' for lead filter runs, an average also, is given in Fig. 9. The fitted line is extrapolated to zero matter (the target plus miscellaneous matter corresponds to 0.70% of a rad. length at $\theta = 83$ mr). It is seen that the vertical intercept is non zero. The horizontal intercept is $(1.4 \pm 0.1)\%$ of a radiation length. This is the evidence that directly produced electrons are observed. A large but uninteresting source of directly produced electrons is the $\pi^0 \rightarrow \gamma e^+ e^-$ Dalitz decay of the π^0 (and similarly for the η^0). Ignoring the η^0 for now (see Sec. V and Appendix VI for this), we subtract the electrons from π^0 Dalitz decay. This is discussed in detail in Appendix VI .

Using the known branching ratio and the measured spectrum of electrons from γ conversions (given the slope of the converter curve), the subtraction is made by further extrapolating 0.82% of a radiation length. This 0.82% includes 0.76% corresponding to the branching ratio and 0.06% corresponding to a small correction due to the fact that the Dalitz photon has a finite small mass. It should be emphasized that this subtraction is in effect measured automatically in this same experiment, the only input is the branching ratio of the π^0 Dalitz decay since the geometry and the kinematics of external and internal conversion are so similar.

The resulting intercept is $(0.6 \pm 0.1)\%$ and represents directly produced electrons without the π Dalitz decay contribution.

The horizontal intercept can be interpreted as the amount of converter one must put into the photon beam to produce these electrons. We call it therefore the e/π^0 ratio (ignoring for the moment other sources of photons such as η^0).

Such extrapolations are made for each running condition, that is at fixed angle in the laboratory and fixed current in the magnet, in bins of P_T . The bin size is 0.2 GeV/c. Binning in P_T rather than P has the advantage that the θ dependence of the yield is smaller. Dalitz pairs are subtracted in all results that are reported below.

B. Results

To calculate the invariant cross section, we need the acceptance of the spectrometer, the electron detection efficiency, targeting efficiency and number of incident protons. We will start giving results (the $e/\pi^0 e$ ratio and the charge asymmetry) which are independent of all these. The results of the two parallel analyses using type 1 cut and type 2 cut (see IV.A.4) are in good agreement (see Sec. IV.C). We therefore use type 1 cut results below.

1. The $e/\pi^0 e$ Ratio and the Charge Asymmetry

The horizontal intercepts of the converter curve as a function of P_T are given for positive and negative electrons

in Fig. 10 and 11 for $\theta = 56$ and 83 mr respectively, corresponding to 65° and 93° in the proton nucleon center of mass. In Fig. 12, the charge asymmetry $(e^+ - e^-)/(e^+ + e^-)$ is given. This is derived directly from the horizontal intercepts by taking the ratio of the difference and the sum of the horizontal intercepts. The e/π^0 ratio and the charge asymmetry have negligible systematic error because the direct electrons are normalized to π^0 electrons which are measured simultaneously with the same acceptance, triggering levels, beam spill structure etc. Because these quantities are ratios, no intensity monitor or targeting efficiency comes into the calculations. Therefore systematic differences in the normalization, acceptance, etc. between the positive and negative settings of the magnet have no effect.

There is no evidence of bumps or charge asymmetry. The significance of the latter is discussed in Sec. V. We therefore average positive and negative electron yields from now on.

2. The Invariant Cross Section

In order to get the invariant cross section from the observed vertical intercept e'/h' of the converter curve, we must know i) the geometric acceptance $A(P_T)$ of the apparatus. This is calculated in Appendix IV, see also Fig. 5 for a typical acceptance using bin size $\Delta P_T = 0.2$ GeV/c.

ii) The efficiency $E_F(P_T)$ for detecting electrons. E_F is the product of the triggering efficiency (Sec. IV.C), reconstruction efficiency (see Secs. IV.A, C) and the cut efficiency (see IV.C).

iii) The value of h' per incident proton (h'/SEM) because the vertical intercept of the converter curve is in units of h' , SEM is defined in Sec. II.

iv) The targeting efficiency η (Sec. II).

v) The deadtime τ caused by the electronics (Sec. III).

The absolute value of the invariant cross section per nucleon is calculated in standard fashion:

$$E \frac{d^3\sigma}{dp^3} \Big|_{\text{per nucleon}} = \frac{1}{9} \left(\frac{e'}{h'}\right) \left(\frac{h'}{SEM \times \tau}\right) \frac{1}{\eta \tau} \frac{1}{E_F} \frac{\sin^2 \theta_{LAB}}{P_T} \frac{1}{A(P_T) \Delta P_T}$$

where A is the number of beryllium nuclei/cm² and the other symbols are defined above.

In the experiment, beryllium ($A = 9$) was used as a target. To get a cross section per nucleon, we divided by 9 thus ignoring a possible A dependence of the cross section.

The invariant cross section $E \frac{d^3\sigma}{dp^3}$ per nucleon as a function of P_T is given in Fig. 13 for 50 and 83 mr and 300 GeV incident protons. It falls smoothly 4 decades in the P_T range from 1.8 to 4.0 GeV/c. In Fig. 14, we give the cross section for electrons produced by photon conversions

per 1% of a radiation length. This is derived from the slope of the converter curve as function of P_T . From this one can derive the π^0 spectrum.¹⁷ This is discussed in Appendix VI. It is shown there that 1% of a radiation length corresponds to an π^0/e ratio of 4000 to 7000 as P_T runs from 2 to 5 GeV/c. See Ref. 17 for a detailed discussion of this.

Figures 10 and 11 show that the directly produced electrons can be simulated by $\sim 0.9\%$ and 0.45% of a radiation length at 50 and 83 mr respectively, roughly independent of P_T . Therefore the e/π^0 ratio is roughly 1.6×10^{-4} and 8×10^{-5} at $\theta_{LAB} = 50$ and 83 mr, respectively.

C. Studies

1. Introduction

In this section, we discuss the issues that came up in A: trigger bias, reconstruction efficiency bias, cut efficiency, fiducial cuts in relation to transverse shower development, pileup in the lead glass calorimeter, πe counter cuts, photon conversions at the walls of the collimator and the shape of the E/P plot for runs with the lead filter.

2. Trigger Bias

Trigger biases introduced by E12L are studied using high statistics runs taken every cycle with $T_O T_M T_1 T_2$ trigger only and a 1.1 radiation length thick lead converter to

increase the number of electrons. The efficiencies of El2I (I = L,M,H) are defined as $T_O T_M T_1 T_2$ El2I/ $T_O T_M T_1 T_2$ and are determined from the slow logic status word. These efficiencies are plotted in Fig. 15 as function of P_T for a typical case (shower cuts of type 1 are applied). The geometric momentum acceptance for electrons is also indicated. It is seen that El2L has reached full efficiency at the beginning of the geometric acceptance. The value of E_c of A4 is indicated. The efficiencies of El2M and El2H are monitored by El2L and El2M respectively. Thus, no trigger bias is present due to threshold effects. The trigger bias introduced by T_2 is negligible. The T_2 pulseheight is plotted in Fig. 16 for events which pass electron cuts using a run with 1.1 cm thick lead converter and for events taken with a $T_O T_M T_1 T_2$ trigger. The arrow indicates where the T_2 discrimination threshold is set (\sim channel 330). It is clear that the T pulseheight for electrons ($>$ channel 400) is larger than the threshold.

3. Reconstruction Efficiency

In A the reconstruction efficiency for electron triggers was given as 80 to 90%. If one assumes that this is true for electrons as well then this number can be used to correct the cross section. The effect of the intensity upon the reconstruction efficiency is given in Table IV. The reconstruction efficiency could be different for different

momenta. This bias is seen to be smaller than 10% as follows. An electron trigger is reconstructed as usual. If the reconstruction is successful, the hodoscope information of the previous random trigger is added to the electron trigger's hodoscope information and another reconstruction is attempted. This second reconstruction of course can fail. The fraction of events that reconstruct the second time is plotted in Fig. 17 as function of P_T . The addition of a random trigger to a standard one changes the reconstruction efficiency by 10 to 30%. From Table IV, one sees that an increase of a factor 4 in the intensity changes the reconstruction efficiency by 10%. We conclude that after the addition of the random trigger, the reconstruction efficiency corresponds to a much larger intensity than we use in the experiment. Therefore the $\pm 10\%$ variation in reconstruction efficiency as function of P_T is an upper limit.

4. Shower Cut Efficiency

The efficiencies of the cuts 1 and 2 of A are studied using runs taken with a converter and with the lead filter, taken with a standard electron trigger. An electron sample (guaranteed electron signal) is obtained by making the usual subtraction. This subtraction is done before and after applying cuts 1 or 2. The cut efficiency is obtained by comparing the number of electrons in the sample before and after cuts. The results are given in Fig. 18 for cut 1.

Of course, the statistical precision is poor at the higher transverse momenta. These cut efficiencies are used in the calculation of the cross section.

The choice of the particular set of type 1 and 2 cuts used in Sec. IV.A is the result of a study of these and other cuts and also of combination of cuts. For example, instead of exploiting the characteristics of the longitudinal shower development, one might use the lateral shower development. One expects hadronic showers to spread more than an electromagnetic shower. Figure 19 shows a typical E/P distribution with and without such a cut on lateral spread. The cut required that not more than 8 % of the shower's energy was deposited outside its core of 10 cm diameter. We have chosen not to use this cut because its hadron rejection is dependent upon the point of incidence on the lead glass calorimeter.

One might consider a combination of cuts. However, there is a considerable overlap between the various types of cuts, for example, after applying the type 2 cut (see Sec. IV.A), the addition of a longitudinal shower cut increases the hadron rejection only slightly. The consistency of the two parallel analyses can be seen from Fig. 20 where the cross sections at 83 mr are plotted for cuts type 1 and 2, respectively.

5. Fiducial Cuts

The fiducial cuts on the lead glass calorimeter must make sure that no energy escapes from the side. The diameter of the shower core can be seen from Fig. 21 where the average fractional energy deposition in a particular block is given as function of the position of the track. The diameter of the shower core is seen to be about 6 cm. We have used 10.0 cm core diameter to define which blocks participate in the shower and 7 cm to make the fiducial cut on the lead glass calorimeter. This is a compromise between measuring the energy well and at the same time reducing the pile up.

6. Pile Up

Pile up in the lead glass calorimeter is due to the fact that the gate for the pulse area digitizers is 250 ns. This is forced essentially by the characteristics of the RCA 8055 photomultiplier used. During this time, extra particles may enter the glass and deposit additional energy. The amount of pile up depends of course upon the intensity and the shower core size one uses to determine which blocks to sum over. This is seen in Fig. 22 where the number of events with a certain fraction of energy deposition outside the standard shower core is plotted. The region outside the shower core is much larger than the core region so we can consider this as an upper limit on how much pile up one has within the core region. Fewer than 20% of the events

have their energy overestimated by more than 6%.

7. πe Requirements

The cut on the number of πe counters (see Sec. II for its definition) firing along a track is chosen with the help of Fig. 23. E/P distributions are shown for a run with a converter to increase the number of electrons with 1, 2 or 3 πe counters respectively firing along a track. We chose to reject events with more than 2 πe firing.

8. Collimator Wall Effects

It is possible that photons striking the precision collimator walls give rise to electrons which could simulate the signal. This is greatly minimized in the design by precisely tapering the limiting collimator, taking advantage of the small size of the photon sources. The collimator walls are lined with heavimet so that any residual wall illumination results in a complete fragmentation of the photon since the small angle shower generation must then pass through a very large number of radiation lengths.

To check on the possible photon conversions at the walls of the collimator, we analyzed part of the data with tighter fiducial cuts on the collimator aperture. No difference was observed in the ratio of the directly produced electrons and conversion electrons (that is the horizontal intercept of the converter curve). We also moved the target off center sideways and looked for a possible illumination of the opposite collimator wall. This would show up as an enhanced yield of electrons from the wall. No such

enhancement was observed. Therefore, we conclude that wall conversions are negligibly small.

9. Lead Filter Effects

To investigate the effects of multiple scattering and hadron absorption in the lead filter, we took some data with 7.6 instead of 5.1 cm lead filter. The shapes of the E/P plots are identical. This shows that these effects are not important and that no electrons exit from the 5.1 cm lead filter which survive the magnetic analysis.

V. INTERPRETATION OF RESULTS AND CONCLUSIONS

A. Summary of Results

1. We have observed directly produced electrons from the reaction $p\text{Be} \rightarrow e^+ + \text{anything}$.
2. There is no evidence of charge asymmetry.
3. The invariant cross section for this reaction is smoothly falling as a function of P_T without evidence of a bump.
4. The ratio of directly produced electrons to pions does not depend very much upon P_T and is about 10^{-4} .
5. Within a factor of 2, the ratio of directly produced electrons to pions is independent of angle.

If we consider other experiments¹⁸, then we may further add:

6. The production of direct electrons and muons is equal within 30%.
7. The production of direct electrons is independent¹⁹ where s is the square of the center of mass energy.

8. The production of muons appears to have the same dependence upon atomic number of the target as hadrons.

B. Sources of Leptons

The possible sources of the electrons divide themselves naturally into two classes: short-lived (the parent decays in the target or very close to it) and long lived. Table V gives estimates of the electron yields from the most important long lived sources in units of Dalitz pairs. The yields are calculated in Appendix VII. The production spectrum for π is assumed to be given by the fit of Ref. 20. The K yield is derived from the π yield using the K/ π ratios of Ref. 21. None of these sources can account for the observed yield. The reason for this is 3-fold: a small branching ratio for decay into electrons, a lifetime such that only a fraction decays in flight between the target and the first analysis magnet and 2 or 3 body decay suppression. The last effect is due to the fact that in order to produce an electron with a given P_T , the parent particle must be produced with a larger P_T . Because the production cross section is a steeply falling curve as a function of P_T , this gives rise to a large suppression (for example, 300 in the case of $K \rightarrow \pi e \nu$).

With regard to the class of short lived particles: The only known sources that could contribute are the vector mesons, the η Dalitz pairs and sources more speculative such as the intermediate vector boson W^\pm ,⁴ the Lee-Wick pole

B^0 ,⁸ Weinberg's Z , ϕ ,⁹ heavy leptons,¹¹ charmed particles,¹³ and virtual photons.²

C. Known Sources: Vector Mesons, η 's, Virtual Photons

Table VI gives estimates for some of these, see Appendix VI. The contribution from vector mesons depends upon their production cross section at large P_T . At present, this is not known. The electron yield from these sources is estimated using their branching ratios into leptons from Ref. 14. In the limit of $SU(6)$ symmetry one expects three ρ, ω, ϕ for each π . This and the fact that the ratio of direct electrons to pions does not depend much on P_T (result 4 above) leads one to suspect that a large fraction of the observed yield comes from vector mesons. To explain the yield this way, one must assume that the vector mesons are produced copiously at large P_T .

The vector mesons give rise to pions and kaons through their decay. This places a limit on the ratio of vector mesons and pions. Assume that the production cross sections are given by $\sigma(\omega) = \sigma(\phi) = \sigma(\rho^0) = N\sigma(\pi^0) = N\sigma(\pi^+) = N\sigma(\pi^-)$; a self consistent solution gives: $N \approx 4$ to 6 depending somewhat on the shape of the production cross section. In this way, the ρ , ω , and ϕ can account for all of the directly produced leptons, see Appendix VI and Table VI. Of course, this must be confirmed by direct detection of ρ , ϕ , ω . The branching ratio of the η^0 into Dalitz pairs is different from that of the π^0 . Therefore, an additional subtraction is necessary as given in Table VI and Appendix VI. Its magnitude

depends upon the production cross section at large P_T of the η^0 which is not known. If η^0 is produced as often as π^0 , the extra subtraction is 15% in π^0 Dalitz decay units. We have made no additional subtraction. The production of virtual photons gives rise to electrons as discussed in Sec. I. The parton model² gives a cross section for this as plotted in Fig. 24 (the curve labeled γ_V). This curve is calculated from the equations of the fourth paper of Ref. 2.

It is assumed that a parton-antiparton annihilation takes place that produces a virtual photon (this is the Drell-Yan mechanism). The antiparton distribution is cut off smoothly at $x = 0.1$ in accordance with the latest results of ν scattering. It is clear that especially at low P_T , this mechanism cannot account for the observed yield. Therefore, we are not sensitive to parton distribution as it was stated too optimistically in Sec. I. The production of a heavy resonance would give rise to a bump superposed upon the continuum under the conditions stated in the introduction. The magnitude of the bump is model dependent. It would appear as an enhancement at a P_T equal to half the mass of the resonance. This is illustrated for the case of W production below and in Appendix VI.

D. Intermediate Bosons

The lepton pair production by a virtual photon is related to W^\pm production using CVC and assuming that the vector and axial vector parts of the interaction hamiltonian contribute equally.

Assuming a branching ratio of $1/4$ for the $W \rightarrow e\nu$ decay, the resulting bump rises from the continuum labeled γ_V in Fig. 24 up to the curve labeled W^\pm at $P_T = M_W/2$. An example is shown for $M_W = 10 \text{ GeV}/c$. The data show no evidence of any bump, see Figs. 10, 11, and 13. If one assumes that the curve γ_V correctly represents the virtual photon contribution (so the observed yield is mainly due to some other source), the following mass limits result: $M_W < 5 \text{ GeV}/c^2$ or $M_W > 11 \text{ GeV}/c$. We want to emphasize that these limits are model dependent and rest on many assumptions. Especially the virtual photon contribution could be smaller, thereby changing these limits. The production of a charged W can give rise to a charge asymmetry. In the p -Be collision, the average charge per nucleon is positive initially ($1/2 e$). If a W is produced, one might expect therefore more W^+ than W^- and therefore an excess of e^+ over e^- . No such excess is seen, see Fig. 12. Of course, if the electron yield is dominated by vector mesons, a possible excess will be washed out because vector mesons produce equal numbers of positive and negative electrons. The absence of bumps and the general shape of the distribution also argue against W^0 , Z^0 , or ϕ as a dominant source.

E. Anomalous Interactions

The unexpected high yield of hadrons from e^+e^- clashing beams has led to speculations about an anomalous lepton hadron interaction.²² Such a new interaction would increase

the electron yield because in addition to the graph of Fig. 1, the graph of Fig. 25 will contribute. Its contribution depends upon the unknown coupling constant of the lepton-x-parton vertex. This may well be idle speculation but it illustrates that the unexpected high yield of electrons in this experiment may lead to new theoretical ideas.

ACKNOWLEDGMENTS

I wish to acknowledge the great effort and dedication of the people of the Columbia-Fermilab Group through which this experiment could be brought to a successful conclusion. It is a pleasure to mention Prof. J.A. Appel, Drs. M.H. Bourquin, D.H. Saxon, and Mr. I. Gaines, all of whom played an essential role in the design, building and testing of the equipment. I wish to thank especially Dr. Jean-Paul Repellin whose great patience, talents and guidance were of great value to me. Prof. Leon M. Lederman deserves special thanks for showing me the way in the labyrinth of high energy physics. His inventiveness and intuition for what is important in physics were crucial. Without the efforts of the staff of the Nevis Laboratories, the staff of the Fermilab, especially the proton laboratory staff, the experiment would not have been possible. I thank Ms. Ann Therrien for the typing of the manuscript.

My wife, Netty, has supported me at all times. Her love and understanding enabled me to go on and finish this work.

APPENDIX I

The Momentum Resolution

The hodoscope strips of H_1 and H_2 are 1.9 cm wide and overlap as shown in Fig. 26. The spatial resolution $D = 0.634$ cm .

$$p = \frac{0.3 \int B d\ell}{\alpha} = 0.3\beta \frac{I}{\alpha}$$

with p the particle's momentum in GeV/c, $\int B d\ell$ the line integral of the magnetic field, α the deflection of the particle in the magnetic field in radians, I the current in the magnet in ampere, $\beta = \int B d\ell / I$.

$$\frac{\sigma_p}{p} = \frac{\sigma_\alpha}{\alpha} = \frac{\sigma_{\alpha p}}{\beta I} .$$

σ_α is only dependent upon D so $\sigma_p/p = \delta \frac{P}{I}$. The constant δ is calculated by Monte Carlo technique. Fix $P = 40$ GeV/c, the position of the track at H_1 is chosen at random. Then the tracks position at H_2 is calculated for a certain current I in the magnet. Then it is determined which hodoscope elements fired and the track is assumed to go through the center of the respective hodoscope strips. The momentum p is calculated and histogrammed. The resulting distribution is not gaussian of course, it peaks at $p = 40$ GeV/c. It follows that $\delta = 0.18$ so

$$\frac{\sigma_p}{p} = 0.18 \frac{P}{I} .$$

We have ignored multiple scattering in $H_1UV_1T_0$ scintillators. The multiple scattering angle is of order $4.4/p$ mr while the bending in the analysis magnet is of order $1500/p$ mr so this is justified.

APPENDIX II

The Lead Glass Calorimeter

The most important processes in electromagnetic showers are bremsstrahlung and pair production. Using asymptotic expressions for these processes, analytic solutions to the shower equations have been derived giving the longitudinal and transversal shower development.²³ These describe the average behavior of the showers, the fluctuations in the shower development is an outstanding problem. The longitudinal shower development initiated by an electron with energy E_0 is given by the number of electrons $\pi(E_0, E, t)$ at depth t (radiation lengths) with energy between E and $E + dE$.

Analogous quantities are defined for photons and showers initiated by a photon. The equations are rather complicated and will therefore not be reproduced. They are used below and in Appendix V and are given by Eqs. (2.55) to (2.60) of Ref.

23. We need the number of electrons, $\Pi(E_0, E, t)$, with energy larger than E and the track length $Z_\pi(E_0, E, t)$ which is the number of electron x cm in the shower. They are given by

$$\Pi(E_0, E, t) = \int_E^\infty \pi(E_0, E', t) dE' \tag{AII.1}$$

$$Z_\pi(E_0, E) = \int_0^\infty \pi(E_0, E, t) dt = 0.437 \frac{E_0}{E} . \tag{AII.2}$$

The center of gravity of electrons with energy larger than E is given by

$$t_{\pi}(E_0, E) = \frac{\int t_{\pi}(E_0, E, t) dt}{\int \pi(E_0, E, t) dt} = 1.01 \ln \frac{E_0}{E} + 0.03 \quad (\text{AII.3})$$

This equation shows that the shower penetration depth is proportional to $\ln \frac{E_0}{E}$ which is a slowly varying function (t_{π} increases from 7 to 9 as E_0 varies from 5 to 50 GeV). Near the end of the shower the particles have energies of the order of the critical energy ϵ ($\epsilon = 16$ MeV for lead, glass, Table I) where the asymptotic expressions are no longer valid and other processes such as the Compton effect, photoelectric effect and electron scattering become important. This prohibits an analytic solution and Monte Carlo techniques are necessary.²⁴ The particles are followed until they have an energy less than 1.5 MeV. This is not quite sufficient (electrons still give Cerenkov light if their energy is larger than ~ 0.92 MeV) but is much better than the analytic solution which is already unreliable when $E \sim \epsilon$. Because the energies involved in this experiment (10-100 GeV) are much larger than those of Ref. 24 (1-6 GeV), we have fitted the analytic solution and the Monte Carlo calculation by varying E and the absolute normalization of the analytic solution. Figure 27 gives the result. We find $E = 7.5$ MeV and $\pi \rightarrow \pi/2$. The Monte Carlo calculation was done for copper where critical energy $\epsilon = 22.4$ MeV so we assume that the parameter E for our lead glass is $E = 7.5 \times 16/22.4 = 5.3$ MeV.

Now we can use the analytic solution to estimate how deep the lead glass calorimeter has to be. We find using Eq. (AII.2) where upper limit of integration is now variable that for a 100 GeV electron 95% of its energy is contained in the first 18 radiation lengths and 99% within 23 r.l.

The fluctuation in the shower development makes it necessary to increase the depth beyond this. We use 27 radiation lengths. From Ref. 24, a 6 GeV electron shower has 95% of its energy in a core of 5 radiation lengths diameter, 90% within 8 . Experimentally, we find for electrons of ~ 50 GeV, 95% is contained within 4.0 cm (Fig. 21). These dimensions are to be compared with a radiation length (2.36 cm from the lead glass, See Table I). Fiducial cuts applied in the off line analysis ensure that only a small fraction of the energy escapes from the side. We now calculate the charge Q from the photomultipliers.

$$Q = G \eta N_C e \quad (\text{AII.4})$$

$$N_C = 400 \sin^2 \theta_C Z_{\pi}(E_O, E) l_R \quad (\text{AII.5})$$

where G is the photomultiplier gain, small e the electron charge, η is the quantum efficiency of the PM, N_C is the number of Cerenkov photons generated by the shower, $400 \sin^2 \theta_C$ is the number of photons per particle per cm with the frequency response of the photomultiplier and the C spectrum folded in, θ_C is the Cerenkov angle, and l_R the radiation length of lead glass.

Z_{π} can be taken from Eq. (AII.2) but we must divide by 2 due to the result of the fit described above. We get using $\eta = 0.2$ and $G = 3 \times 10^5$

$$N_c = 135 \frac{E_0}{E} \quad (\text{AII.6})$$

$$Q = 1.3 \frac{E_0}{E} \text{ pC} \quad (\text{AII.7})$$

The FWHM of the photomultiplier is 80 ns so for a 5.3 GeV electron ($E_0/E = 1000$) this corresponds to 400 mV into 25 Ω .

We observed 90 mV for a 6 GeV electron. The factor 4 discrepancy is probably due to the uncertainty of the cutoff energy E , uncertainty in the gain G and possible light collection inefficiency of the Cerenkov light by the photomultiplier.

Equation (AII.7) expresses that at least in principle the lead glass calorimeter has a linear relationship between the energy of the incident electron and the pulse area. Special care has been taken in the base design to make sure that the photomultipliers are linear.

A 53 GeV electron produces $\eta N_c = 2.7 \times 10^5$ photoelectrons. This means 0.2% resolution due to photostatistics. The second paper of Ref. 15 gives an extrapolated σ_E/E of $\sim 1\%$. It is clear that photostatistics do not contribute significantly to the resolution. If we assume that the number of photoelectrons is four times lower (see above) the resolution is 0.4% due to photostatistics. This does not alter the conclusion.

G has been measured using a light flasher. Because its pulse height has large fluctuations (30%), a trick was applied. The output pulses of two photomultipliers viewing the same light flasher have been integrated and fed into two pulse height analyzers. For each light flash the ratio R of the two pulse heights was calculated and histogrammed. This ratio is stable although the light flasher pulse height is not.

We assume that the standard deviation σ of R is due to photostatistics only and not for example due to a different non-linearity of the two photomultipliers. We observe $\sigma_R/R = 1.0 \times 10^{-2}$, so each tube has photostatistics of $\frac{\sigma}{N} = \frac{1}{\sqrt{N}} = \frac{1}{\sqrt{2}} \frac{\sigma_R}{R}$ where N is the number of photoelectrons. It follows that $N = 2R^2/\sigma_R^2 = 2 \times 10^4$. Under these conditions, the pulse height and width were 400 mV (into 25 Ω) and 50 ns respectively corresponding to $0.4 \times 50 \times 10^{-9}/25 \sim 10^{-9}$ C so $G = 10^{-9}/(2 \times 10^4 \times 1.6 \times 10^{-19}) = 3 \times 10^5$.

APPENDIX III

The Calibration of the Lead Glass Calorimeter

If a shower distributes energy over n blocks of lead glass, then

$$E = \sum_{i=1}^n C_i H_i \quad (\text{AIII.1})$$

where H_i is the pulse height (channels) in block i and C_i is a proportionality constant called calibration constant of block i (dimension GeV/channel). In order to determine the C_i , we use runs taken at 20 mr in the laboratory with a lead converter in the beam of photons to increase the number of electrons in the beam in a bin of the momentum P , with bin size of the order of the momentum resolution. The energy resolution will be minimized by adjusting C_i , the minimum corresponds to the correct C_i :

$$(\Delta E)^2 = \sum_{i,j=1}^n C_i C_j \Delta H_i \Delta H_j \quad (\text{AIII.2})$$

Average this (for this reason we binned data in P bins):

$$\langle (\Delta E)^2 \rangle = \sigma^2 = \sum C_i C_j \rho_{ij}, \quad \rho_{ij} = \langle \Delta H_i \Delta H_j \rangle. \quad (\text{AIII.3})$$

We call ρ_{ij} the correlation matrix because its off diagonal elements describe the correlations between energy fluctuations in different blocks. They would be zero if these fluctuations are independent. Its diagonal elements are the squares of standard deviation of H_i . We minimize σ^2 with the constraint that

$$\langle E \rangle = \sum_i C_i \langle H_i \rangle \quad . \quad (\text{AIII.4})$$

Introduce Lagrange multiplier λ and minimize $\sigma^2 - \lambda \langle E \rangle$

$$\frac{\partial}{\partial C_i} (\sigma^2 - \lambda \langle E \rangle) = \sum_j [C_j \rho_{ij} - \lambda \langle H_i \rangle \delta_{ij}] = 0 \quad (\text{AIII.5})$$

gives an inhomogeneous linear set of equations which we can solve for all C_i except one. This one can be factored out and is an overall normalization constant whose value follows from Eq. (AIII.4). ρ_{ij} and $\langle H_i \rangle$ can be calculated from the data and the C_i calculated. We do this for each layer of lead glass for different bins in momentum and for different magnet currents to check its consistency and linearity. There is good agreement between the different conditions. It is possible to assign an absolute calibration number using muon straightthroughs.

A muon deposits energy in the lead glass, the amount of which is independent of its energy. It depends upon the direction of the track and its position with respect to the photomultiplier that collects the light. If these conditions are standardized, a change in a calibration constant (because a photomultiplier gain changes with time say) is reflected in a change in the average pulse height $\langle H_i \rangle^\mu$ of block i . We require $\langle H_i \rangle^\mu \times C_i = b_i$.

The constants b_i are determined once and for all for each block using a muon and electron run taken very close together in time.

The calibration constants drift up by an estimated ~ 1% per month. This is very likely due to the gains of the photomultipliers.

APPENDIX IV

The Geometric Acceptance

The geometric acceptance of the spectrometer is determined by the fiducial cuts that have been applied to the data. These cuts are tighter than the cuts introduced by the physical limitations due to apertures, hodoscope edges, etc. The fiducial cuts given in Sec. IV.A are used in the acceptance calculations.

The acceptance is calculated as follows. We chose 3 independent variables $(P_T, \cos\theta, \phi)$ rather than $(P, \cos\theta, \phi)$ say because in the first case the θ dependence of the yield is smaller. This will be exploited in integration over $\cos\theta$ below. Three variables are sufficient if we ignore the finite size of the target. The number of observed particles N is (apart from a constant)

$$N = \int dP_T \int d\cos\theta \int d\phi A(P_T, \cos\theta, \phi) \frac{d\sigma}{dP_T d\cos\theta d\phi}$$

where $d\sigma/dP_T d\cos\theta d\phi$ is the production cross section and $A(P_T, \cos\theta, \phi)$ is the probability that a particle that originates from the target with $(P_T, \cos\theta, \phi)$ is accepted. If we ignore multiple scattering in the helium gas converters and hodoscopes, A is either 0 or 1. The integral over ϕ can be done without making any further assumptions because the production cross section is independent of ϕ .

To do the integral over $\cos\theta$, we assume that $d\sigma/dP_T d\cos\theta d\phi$ is constant over the accessible range. Because the limits of the integration are complicated functions of

P_T and $\cos\theta$, the integration is done using a Monte Carlo technique. The finite momentum resolution is introduced as a gaussian smearing with a standard deviation from Appendix I. It has a large effect near the onset of the acceptance. An acceptance is plotted in Fig. 5 for a typical spectrometer setting.

APPENDIX V

Electromagnetic Feedthrough Through Thick Filters

The background subtraction using the lead filter runs plays a crucial role in the analysis. One must be sure that indeed no electrons exit from the downstream end of it.

To calculate the flux of electrons from such a filter we use the equations for the longitudinal shower development of Ref. 23. They are discussed briefly in Appendix II.

We assume a spectrum of incident electrons according to $\frac{d\sigma}{dE_0} = e^{-3.4P_T}$ with E_0 the energy of the electron. Then

$$\frac{dN}{dE} = \frac{1}{2} \int_0^{\infty} \pi(E_0, E, t) \frac{d\sigma}{dE_0} dE_0$$

is the number of electrons of one sign at depth t radiation lengths, π is defined in Appendix II. This is plotted in Fig. 28.

The number of electrons of one sign with energy larger than 30 GeV is given by $\int_{30}^{\infty} \frac{dN}{dE} dE$ and plotted in Fig. 29 as a function of the thickness of the filter in units of electrons from 100% γ conversion. The directly produced electron yield corresponds to about 1% of a radiation length at $\theta = 50$ and 0.5% at $\theta = 83$. From Fig. 29, it is clear that the feedthrough is down by $> 10^5$ from the $\pi^0 e$ yield and can therefore be neglected. It should be emphasized that the analytic shower theory is very accurate in this application because the energies involved are larger than 30 GeV so the approximations discussed in the beginning of Appendix II are justified.

APPENDIX VI

Short Lived Electron Sources

We have investigated all known sources of electrons. They divide themselves naturally into 2 classes: long lived (parent decays in flight between target and spectrometer) and short lived (parent decays in the target). The first class is discussed in Appendix VII. Here we will concentrate on the second class.

We start with the process $\pi^0 \rightarrow \gamma\gamma$.

$$\frac{dn}{dE_\gamma} = \frac{2}{E_\pi} , \quad \frac{E_\pi - P_\pi}{2} \leq E_\gamma \leq \frac{E_\pi + P_\pi}{2} ,$$

where dn/dE_γ = probability to find a γ with energy between E_γ and $E_\gamma + dE_\gamma$ and E_π is the π^0 energy, all quantities are lab variables. The π^0 production spectrum is taken from Ref. 20 which is in excellent agreement with the π^0 spectrum as measured in this experiment.^{17,25} In Fig. 30, π^0 as well as γ spectrum is plotted. The γ spectrum is down by a factor of 5 from the π^0 spectrum for P_π between 2-4 GeV/c. Twice this factor we call R_2 , the 2 body decay suppression. Twice because there are two identical particles in the final state. The spectrum of electrons of one sign that results from 100% γ conversion is given by Ref. 23.

$$P(E_e, E_\gamma) = \left[\left(\frac{E_e}{E_\gamma}\right)^2 + \left(1 - \frac{E_e}{E_\gamma}\right)^2 + \left(\frac{2}{3} - 2b\right) \frac{E_e}{E_\gamma} \left(1 - \frac{E_e}{E_\gamma}\right) \right] \frac{dE_e}{E_\gamma}$$

where the energy of the electrons is between E_e and $E_e + dE_e$, $b^{-1} = 18\alpha n(183Z)^{-1/3}$. Z is the atomic number

of the converter. (Because b is negligible, the exact value of z has no effect on the result.) Figure 30 gives the spectrum of electrons of one sign from 100% γ conversion. The ratio π^0/e is a function of P_T . The spectrum of e from $\pi^0\gamma$ conversion can be determined from the slope of the converter curve. Then the π^0 spectrum follows. This is the subject of the thesis of I. Gaines.¹⁷

The π Dalitz decay $\pi^0 \rightarrow \gamma e^+ e^-$ follows from $\pi^0 \rightarrow \gamma\gamma$ using the branching ratio $B_\pi = \pi^0 \rightarrow \gamma e^+ e^- / \pi^0 \rightarrow \text{all} = 1.17 \times 10^{-2}$. If one ignores the effect of the mass of the internally converted photon, the spectrum of these electrons is down from 100% converted $\pi^0 \gamma$'s by $B/2$ conversion lengths or $B_\pi/2 \times 9/7 = 0.76 \times 10^{-2}$ radiation lengths. To take the mass of the converted photon into account we use the results of Ref. 26. Two variables x and y are introduced, the energy E_+ of the positron and E_- of the electron are given by

$$E_+ = (x^2(1-y) + m_e^2(1+y))/4m_e$$

$$E_- = (x^2(1+y) + m_e^2(1-y))/4m_e$$

and the probability distribution $\rho(x,y)$ of x and y is

$$\rho = \frac{\alpha}{2\pi} \int_{\frac{2m_e}{E}}^{\frac{E}{x}} \frac{dx}{x} \int_{-\eta}^{\eta} dy \left(1 - \frac{x^2}{E^2}\right)^3 \left(1 + y^2 + \frac{4m_e^2}{x^2}\right)$$

$$\eta = \left[1 - \left(\frac{2m_e}{x}\right)^2\right]^{1/2}$$

A Monte Carlo program calculates the yield of electrons of one sign. The ratio between these electrons and the electrons produced by 0.76×10^{-2} RL converter is (1.08 ± 0.04) independent of P_T . We conclude therefore that π^0 Dalitz decay electrons can be subtracted by extrapolating to -0.82×10^{-2} RL.

The $\eta^0 \rightarrow \gamma\gamma$ with subsequent conversion in the target or other matter is subtracted out correctly by the extrapolation to zero matter. We do not need to know the η^0 production cross section for this. Some of the electrons from η Dalitz decay modes are still included because

$$B_{\eta} = \frac{\eta^0 \rightarrow e^+e^-\gamma}{\eta^0 \rightarrow \text{all}} = 1.62 \times 10^{-2} \quad . \quad 27$$

Therefore an additional subtraction must be made which, in units of π^0 Dalitz decay electrons, is equal to

$$\left(\frac{\eta}{\pi^0}\right) \frac{\eta \rightarrow \gamma\gamma}{\eta \rightarrow \text{all}} \frac{B_{\eta} - B_{\pi}}{B_{\pi}} = 0.146 \left(\frac{\eta}{\pi^0}\right)$$

where (η/π^0) is ratio of the production cross sections of η and π . We have done no such subtraction in the analysis because the production cross section at high P_T of the η is not known. If $\eta/\pi^0 = 1$, a 15% additional subtraction is necessary. At 83 mr, the directly produced electron signal is about 50% in these units so this would reduce the cross section by factor 2/3. Now it will be shown that vector mesons, in particular ϕ , could account for the observed yield of electrons if ϕ is produced with at least

3 x the cross section as π^0 (strict SU(6)) symmetry requires 3ϕ for every π). For definitiveness, we assume ϕ are produced with the same cross sections as π^0 above. Then the $\phi \rightarrow e^+e^-$ decay mode gives as e energy spectrum down from ϕ by $R_2 = 11$, the 2 body decay suppression factor. The branching ratio

$$\frac{\phi \rightarrow e^+e^-}{\phi \rightarrow \text{all}} = (3.2 \pm 0.3) \times 10^{-4} \text{ times } R_2^{-1}$$

gives e from $\phi \sim 0.21$ in units of π Dalitz decay compared to observed yield of 0.5. In the same way, the ρ and ω yields of Table VI are calculated. However, the e/π results are decreased because ρ^{\pm} add to the pions significantly.

In fact, we can set an upper limit on the ρ contribution. Assume all π come from ρ . Because $(\rho \rightarrow \pi\pi)/(\rho \rightarrow \text{all}) \simeq 1.00$, this means that the production cross section for ρ must be less than 11 times (again 2 body decay suppression) the π production cross section. From Table VI, we see that this gives an upper limit of 0.3 on the electron yield from ρ .

A similar upper limit of 4.5 can be set on ϕ contribution using $\phi \rightarrow KK$. This limit is so much higher because $(\phi \rightarrow K^+K^-)/(\phi \rightarrow \text{all}) = 0.47$ and its branching ratio into e^+e^- is roughly 7.5 times larger. Finally, we want to give an example of what magnitude bump can be produced by a $W \rightarrow e\nu$ or $B^0 \rightarrow e^+e^-$. Reference 7 gives

$$\frac{d\sigma^W}{dP_T} = \frac{2P_T}{M_W \left(\frac{M_W^2}{4} - P_T^2 \right)^{\frac{1}{2}}} \frac{d\sigma}{dM_W} .$$

The cross section averaged over P_T between $P_T = \frac{M_W}{2} - 0.2$ to

$$P_T = \frac{M_W}{2} \text{ is } \sigma = 5 \sqrt{\frac{0.8}{M}} \left\{ \frac{3\pi}{0.09 M^2} \right\} q \frac{d\sigma}{dq^2} \frac{1}{\pi} .$$

Top line is for B^0 production, bottom line for W^\pm production.

For $d\sigma/dq$, we take the results of Ref. 2, third paper. In

a P_T bin of 0.2 GeV/c, we get an enhancement as shown in

Fig. 24 as the difference between the curves labeled γ_V

and B^0, W , respectively.

APPENDIX VII

Long Lived Electron Sources

We will show that no long lived (as defined in Appendix VI) parent particle can give rise to the observed electron yield. The results of the calculations are in Table V.

The reason for this is 2 and 3 body decay suppression factor of Appendix VI and small branching ratios. In addition to these effects (which are present for both long lived and short lived sources), the long lived sources have their electron yield suppressed because of their long lifetime. Because the parent particle must decay upstream of the lead filter position, such lifetimes let only a fraction decay. If the decay is downstream of the filter position most of the resulting electrons will be automatically subtracted in the analysis apart from the fact that $\sim 25\%$ of the hadrons are absorbed in the filter. To study $K \rightarrow \pi^0 e \nu$ and $K_L^0 \rightarrow \pi e \nu$, we used the production spectrum of pions given by Ref. 20. This is in good agreement with the pion spectrum observed in this experiment. To get the kaon production we used the K/π ratios of Ref. 21. A Monte Carlo program produced the required electron spectra with the energy spectrum of the electron in the c.m. of the kaon given by the decay probability²⁸

$$d\omega = \text{constant} \times [2m_K E_e E_\nu - m_K^2 (W_0 - E_\pi)]$$

with W_0 the maximum energy of the pion. E_π , E_e and E_ν the energies of the pion, electron and neutrino respectively.

We assumed that in the laboratory the decay products are collinear with the direction of the parent. But in fact the parent is produced at a slightly smaller angle on the average. This raises all numbers by 30%. The 3 body suppression factor R_3 is about 300 at $P_T = 2.5 \text{ GeV}/c$.

We have for

$$K \rightarrow \pi^0 e \nu \left(\frac{e^+}{\pi^+} \right)_{K^+} = \frac{K^+}{\pi^+} \frac{K \rightarrow \pi^0 e \nu}{K \rightarrow \text{all}} \frac{L}{\gamma c \tau_K} \frac{1}{R_3}$$

$$K_L^0 \rightarrow \pi e \nu \left(\frac{e^+}{\pi^+} \right)_{K^0} = \frac{K_L^0}{\pi^+} \frac{1}{2} \frac{K_L^0 \rightarrow \pi e \nu}{K_L^0 \rightarrow \text{all}} \frac{L}{\gamma c \tau_{K^0}} \frac{1}{R_3}$$

The factor 1/2 accounts for the fact that only half of the $K^0 \rightarrow \pi e \nu$ decays gives an electron with the correct charge.

Using $K_L^0/\pi^+ = 0.35$, $L = 7 \text{ m}$, $\gamma = 50$ (25 GeV kaons),

$c \tau_K = 3.71 \text{ m}$, $c \tau_{K^0} = 15.5 \text{ m}$, $K^+ \rightarrow \pi e \nu / K \rightarrow \text{all} = 4.85 \times 10^{-2}$.

$$\frac{K^0 \rightarrow \pi e \nu}{K^0 \rightarrow \text{all}} = 0.39, \text{ we get}$$

$$\left(\frac{e^+}{\pi^+} \right)_{\pi^+ K^+} \sim 3 \times 10^{-6}$$

$$\left(\frac{e^+}{\pi^+} \right)_{\pi^+ K^0} \sim 2 \times 10^{-6}$$

Similarly for $K^- \rightarrow \pi^0 e \nu$

$$\left(\frac{e^-}{\pi^- K^-}\right) \sim 1 \times 10^{-6} .$$

In Table IV these are expressed in units of π^0 Dalitz decay electrons, e_d , using $e_d/\pi^0 = 2 \times 10^{-4} \times 0.82 = 1.6 \times 10^{-4}$, see Appendix VI.

The hyperon production is assumed to be smaller than K production. Their branching ratio into leptons is more than a factor 10 smaller than the kaons. Therefore, they contribute less than 10^{-3} .

The $K_S^0 \rightarrow \pi^0 \pi^0$ is of interest because it may lead to an underestimation of the directly produced electron yield. It is a source of π^0 which is automatically oversubtracted by the extrapolation to zero matter. Over subtracted because the photons from π^0 decay cannot convert in the target due to the γct_K of K^0 . However this effect is negligible.

$$\frac{e^+}{\pi^+} = \frac{K_S^0}{\pi^+} \frac{K_S^0 \rightarrow \pi^0 \pi^0}{K_S^0 \rightarrow \text{all}} \frac{(\pi^0 \rightarrow e) \text{ 1\% conv}}{R_2} .$$

Using $K_S^0/\pi^+ = 0.35$, $R_2 = 7$ from a Monte Carlo (7 instead of 5.5 for $\pi^0 \rightarrow \gamma\gamma$ because m_π is not negligible with respect to m_K), $\pi^0 \rightarrow e$ for 1% conversion probability (the amount of matter in the target is less than that) is 2×10^{-4} ,

see Appendix VI.

$$\frac{K_S^0 \rightarrow \pi^0 \pi^0}{K_S^0 \rightarrow \text{all}} = 0.31 , \text{ we get}$$

$$\frac{e^+}{\pi^+} = 3 \times 10^{-6}$$

a in π^0 Dalitz decay units 2×10^{-2} . This is negligible. For the $\mu \rightarrow e\nu\nu$ decay, we have a 3 body decay suppression factor $R_3 = 120$, $L/\gamma c\tau_\mu = 5 \times 10^{-5}$ with $\gamma = 200$ (20 GeV/c muon) so $e/\mu = 4 \times 10^{-7}$. The muon yield is down from the pion yield by factor $L/\gamma c\tau_\pi \sim 10^{-2}$ because of pion lifetime and by a two body decay suppression factor so we get

$$\left(\frac{e}{\pi}\right)_\mu \leq 4 \times 10^{-9} \quad [2 \times 10^{-5} \text{ in } \pi^0 \text{ Dalitz decay units}]$$

This is negligible.

For $\pi \rightarrow e\nu$, we have 2 body suppression $R_2 = 11$, $L/\gamma c\tau_\pi \approx 10^{-2}$ and a branching ratio 1.2×10^{-4} , so

$$\left(\frac{e}{\pi}\right) = 1.5 \times 10^{-7} \quad (10^{-3} \text{ in } \pi^0 \text{ Dalitz decay units}).$$

REFERENCES

- 1 J.H. Christenson, G.C. Hicks, L.M. Lederman, P.J. Limon, B.G. Pope, E. Zavattini, Phys. Rev. D8, 2016 (1973).
- 2 S.D. Drell, T.M. Yan, Phys. Rev. Lett. 25, 316 (1970).
R.W. Fiddler, Phys. Lett. 46B, 455 (1973).
H.P. Paar, E.A. Paschos, Phys. Rev. D10, 1502 (1974).
G.R. Ferrar, Cal Tech Preprint CALT-68-22.
R. Savit, M.B. Einhorn, Phys. Rev. Lett. 33, 392 (1974).
- 3 H. Yukawa, Proc. Phys.-Math. Soc., Japan 17, 48 (1934).
- 4 T.D. Lee, C.N. Yang, Phys. Rev. Lett. 4, 307 (1960).
C.H. Llewellyn-Smith, CERN Summer Study (1972).
G. Feinberg, Phys. Rev. 134B, 1255 (1964).
R.E. Marshak, R.N. Mohapatra, S. Okubo, J. Subba Rao, Proceedings of the CERN 1969 Conference on Weak Interactions (CERN 69-7).
S. Okubo, Nuovo Cimento A54, 491 (1968).
S. Okubo, Nuovo Cimento A57, 794 (1968).
C. Ryan, S. Okubo, R.E. Marshak, Nuovo Cimento 34, 753 (1964).
S. Okubo, C. Ryan, R.E. Marshak, Nuovo Cimento 34, 759 (1964).
C.G. Callen, Phys. Rev. Lett. 20, 809 (1968).
T. Ericson, S.L. Glashow, Phys. Rev. 133, B130 (1964).
S.V. Pepper, C. Ryan, S. Okubo, R.E. Marshak, Phys. Rev. 137, B1259 (1965).

5 Neutrino produced W:

M.M. Block, H. Burmeister, D.C. Cundy, B. Eiben, C. Franzinetti, J. Keren, R. Møllerud, G. Myatt, M. Nikolic, A. Orlin-Lecourtois, M. Paty, D.H. Perkins, C.A. Ramm, K. Schultze, H. Sletten, K. Soop, R. Stump, W. Venus, H. Yoshiki, Phys. Lett. 12, 281 (1964).

C. Bernardini, H. Bienlein, A. Böhm, G. von Dardel, H. Faissner, F. Ferrero, J.M. Gaillard, H.J. Gerber, B. Hahn, M. Holder, V. Kaftanov, F. Krienen, C. Manfredotti, M. Reinharz, R.A. Salmeron, A. Stande, H.J. Steiner, J. Bartley, M.M.

Block, H. Burmeister, D.C. Cundy, B. Eiben, C. Franzinetti, J. Keren, R. Møllerud, G. Myatt, M. Nikolic, A. Orbin-Lecourtois, M. Paty, D.H. Perkins, C.A. Ramm, K. Schultze, H. Sletten, K. Soop, R. Stump, W. Venus, H. Yoshiki, Nuovo Cimento 38, 608 (1965).

B.C. Barish, J.F. Bartlett, D. Buchholtz, T. Humphrey, F.S. Merrit, Y. Nagashima, F.J. Sciulli, S. Shields, H. Suter, G. Krafczyk, A. Maschke, Phys. Rev. Lett. 31, 180 (1973).

R. Burns, K. Goulianos, E. Hyman, L. Lederman, W. Lee, N. Mistry, J. Rettberg, M. Schwartz, J. Sunderland, Phys. Rev. Lett. 15, 42 (1965).

pN Produced W:

R. Burns, G. Danby, E. Hyman, L.M. Lederman, W. Lee, J. Rettberg, J. Sunderland, Phys. Rev. Lett. 15, 830 (1965).

C.M. Ankenbrandt, R.C. Larsen, L.B. Leipuner, L.W. Smith, P.J. Wanderer, R.J. Stefanski, H. Kasha, R.K. Adair, Phys. Rev. D3, 2582 (1971).

- R.C. Lamb, R.A. Lundy, T.B. Novey, D.D. Yovanovitch,
M.L. Good, R. Hartung, M.W. Peters, A. Subramarian, Phys.
Rev. Lett. 15, 800 (1965).
- ⁶ B.C. Barish, J.F. Bartlett, D. Buchhaltz, F.S. Merrit,
F.J. Sciulli, D. Shields, H. Suter, G. Krafczyk, Phys.
Rev. Lett. 32, 1387 (1974).
- ⁷ L.M. Lederman, B.G. Pope, Phys. Rev. Lett. 27, 765 (1971).
L.M. Lederman, D.H. Saxon, Nucl. Phys. B63, 313 (1973).
- ⁸ T.D. Lee, G.C. Wick, Phys. Rev. D2, 1033 (1970).
- ⁹ S. Weinberg, Phys. Rev. Lett. 19, 1264 (1967).
S. Weinberg, Phys. Rev. D5, 1412 (1972).
S. Weinberg, Phys. Rev. Lett. 24, 1688 (1971).
A. Salam in Elementary Particle Theory, ed, by N. Svartholm
(Almquist and Forlag, Stockholm 1968), p. 367.
- ¹⁰ H. Georgi, S.L. Glashow, Phys. Rev. Lett. 28, 1494 (1972).
- ¹¹ B.W. Lee, Phys. Rev. D6, 1188 (1972).
J. Prentki, B. Zumino, Nucl. Phys. B47, 99 (1972).
- ¹² F.J. Hasert, S. Kabe, W. Krenz, J. von Krogh, D. Lanske,
J. Morfin, K. Schultze, H. Weerts, G.H. Bertrank-Coremans,
J. Sacton, W. vanDoninck, P. Vilain, U. Camerini, D.C.
Cundy, R. Baldi, J. Damilchenko, W.F. Fry, D. Haidt,
S. Natali, P. Musset, B. Osculati, R. Plamer, J.B.M.
Pattison, D.H. Perkins, A. Pullia, A. Rousset, W. Venus,
H. Wachsmuth, V. Brisson, B. Degrange, M. Hagnenauer,
L. Kluberg, U. Nguyen-Khac, P. Petiau, E. Belotti, S. Bonetti,

12

cont'd

D. Cavalli, C. Conta, E. Fiorini, M. Rollier, B. Aubert,
D. Blum, L.M. Chonnet, P. Heusse, A. Lagarrigue, A.M.
Lutz, A. Orkin-Lecourtois, J.P. Vialle, F.W. Bullock,
M.J. Esten, T.W. Jones, J. McKenzie, A.G. Michette,
G. Myatt, W.G. Scott, Phys. Lett. 46B, 138 (1973).
A. Benvenuti, D.C. Cheng, D. Cline, W.T. Ford, R. Turlay,
T.Y. Ling, A.K. Mann, F. Messing, R.L. Piccioni, J. Pilcher,
D.D. Reeder, C. Rubbia, R. Stefanski, L. Sulak, Phys.
Rev. Lett. 32, 800 (1974).
S.J. Barish, Y. Cho, M. Derrick, L.G. Hyman, J. Rest,
P. Schreiner, R. Singer, R.P. Smith, H. Yuta, D. Koetke,
V.E. Barnes, D.D. Carmony, A.F. Garfinkel, Phys. Rev.
Lett. 33, 448 (1974).
B. Aubert, A. Benvenuti, D. Cline, W.T. Ford, R. Imlay,
T.Y. Ling, A.K. Mann, F. Messing, R.L. Piccioni, J. Pilcher,
D.D. Reader, C. Rubbia, R. Stefanski, L. Sulak, Phys.
Rev. Lett. 32, 1454 (1974); 1457 (1974).

13

S.L. Glashow, J. Iliopoulos, L. Maiani, Phys. Rev. D2,
1285 (1970).

14

T.A. Lasinski, A. Barbaro-Galtieri, R.L. Kelly, A. Rittenberg,
A.H. Rosenfeld, T.G. Trippe, N. Barish-Schmidt, C. Bricman,
V. Chaloupka, P. Soding, M. Roos, Rev. Mod. Phys. 45,
s1 (1973).

- 15 Y. Hemmi, R. Kikuchi, S. Kobayashi, K. Miyake, T. Nahamura,
H. Okuno, S. Yasumi, Y. Yoshimura, Nucl. Instr. & Meth.
56, 213 (1967).
B.J. Blumenfeld, L.M. Lederman, R.L. Cool, S.L. Segler,
Nucl. Instr. & Meth. 97, 427 (1971).
J.A. Appel, M.H. Bourquin, I. Gaines, D.C. Hom, L.M.
Lederman, H.P. Paar, J.-P. Repellin, D.H. Saxon, H.D.
Snyder, J.M. Weiss, J.K. Yoh, B.C. Brown, J.-M. Gaillard,
T. Yamanouchi, Phys. Rev. Lett. 33, 719 (1974).
- 16 D.H. Saxon, M.H. Bourquin, Nucl. Instr. & Meth. 108, 461 (1973).
- 17 I. Gaines, Thesis, Columbia University, Nevis Report
- 18 J.P. Boymond, R. Mermod, P.A. Piroue, R.L. Sumner,
J.W. Cronin, H.^J. Frisch, M.J. Sochet, Phys. Rev. Lett.
33, 112 (1974).
T. Yamanouchi, Proceedings of the XVII Conference on High
Energy Physics, London (1974).
J.A. Appel, M.H. Bourquin, I. Gaines, D.C. Hom, L.M.
Lederman, H.P. Paar, J.-P. Repellin, D.H. Saxon, H.D.
Snyder, J.M. Weiss, J.K. Yoh, B.C. Brown, J.-M. Gaillard,
T. Yamanouchi, Phys. Rev. Lett. 33, 722 (1974).
- 19 S. Segler, Proceedings of the XVII Conference on High
Energy Physics, London (1974).
- 20 F.W. Busser, L. Camilleri, L. DiLella, G. Gladding, A. Placci,
B.G. Pope, A.M. Smith, J.K. Yoh, E. Zavattini, B.J. Blumenfeld,
L.M. Lederman, R.L. Cool, L. Litt, S. Segler, Phys. Lett.
46B, 471 (1973).

- 21 J.W. Cronin, H.J. Frisch, M.J. Sochet, J.P. Boymond,
P.A. Piroue, R.L. Sumner, Phys. Rev. Lett. 31, 1426 (1973).
- 22 J.C. Pati, A. Salam, Phys. Rev. Lett. 32, 1083 (1974).
- 23 B. Rossi, K. Greisen, Rev. Mod. Phys. 13, 240 (1941).
K. Kamata, J. Nishimura, Prog. Theor. Phys. 8, 93 (1953).
- 24 U. Volkel, DESY Report 65/6 (1965).
U. Volkel, DESY Report 67/16 (1967).
- 25 J.A. Appel, M.H. Bourquin, I. Gaines, D.C. Hom, L.M.
Lederman, H.P. Paar, J.-P. Repellin, D.H. Saxon,
H.D. Snyder, J.M. Weiss, J.K. Yoh, B.C. Brown, J.-M.
Gaillard, T. Yamanouchi, Phys. Rev. Lett. 33, 719 (1974).
- 26 N.M. Kroll, W. Wada, Phys. Rev. 98, 1355 (1955).
- 27 T. Miyazaki, E. Takasuki, Phys. Rev. D8, 2051 (1973).
- 28 L.M. Chonnet, J.-M. Gaillard, M.K. Gaillard, Phys. Reports
4, 199 (1972).
- 29 J.-M. Gaillard, private communication.

Table 1

Lead Glass Properties

Manufacturer	Ohara, Inc. Tokyo
Type	SF 5
Radiation Length	2.36 cm.
Density	4.08 g/cm. ³
Index of Refraction	1.6727
Critical Energy	15.8 MeV

Table 2

Trigger and Cut Statistics

Comparison of runs with and without
5.1 cm. thick lead filter.

θ_{LAB}	83 mrad	83
Magnet Current	600A (negative)	600A (negative)
Converter	none	5.1 cm. lead
SEM/pulse	1.64×10^{11} proton/pulse	1.65×10^{11}
$T_0 T_1 T_M$	3.88×10^8	3.69×10^8
$T_0 T_1 T_M T_2$	2.97×10^6	2.69×10^6
$T_0 T_1 T_M T_2$ (6/6) (1)	2.53×10^6	2.2×10^6
$T_0 T_1 T_M T_2$ (6/6) (πe) (2)	1.83×10^6	1.37×10^6
$T_0 T_1 T_M T_2$ (6/6) (πe) (E12 L) (prescaler = 8)	1.07×10^4	1.20×10^4
E12 M (prescaler = 1)	3.93×10^4	4.40×10^4
E12 H (prescaler = 1)	7.40×10^3	7.59×10^3

For E12 M Trigger only:

On tape(3)	17780	22722
Reconstruct	14377	18930
Before shower cut		
($0.93 \leq E/P \leq 1.07$)	5335	5106
($E/P < 0.93$)	15683	21439
After shower cut		
($0.93 \leq E/P \leq 1.07$)	1614	650
($E/P < 0.93$)	2734	2686

- 1.) 6/6 means that the trigger required >0 particles in every hodoscope plane.
- 2.) πe means that the trigger required <4 πe counters firing along a track.
- 3.) Of the 39300 E12 M events only 17780 are on tape because of the computer deadtime.

Table 3

Reconstruction Statistics

	$\theta = 50$ mrad I=1000A pos. 3×10^{10} p/pulse	$\theta = 83$ mrad I=600 A pos. 1.2×10^{11} p/pulse
Number of triggers	44606	45635
Number of events that reconstruct	36986 (83%)	36187 (79%)
No track to target in horizontal plane	8788 (20%)	9665 (21%)
Too many tracks to target in horizontal plane	1283 (2.9%)	1751 (3.8%)
No consistency between $H_1 M H_2$	1872 (4.2%)	2937 (6.4%)
Too many tracks in $H_1 M H_2$	1025 (2.3%)	1251 (2.7%)
No $H_1 U V_1$ consistency	136 (0.3%)	246 (0.5%)
Too many $H_1 U V_1$ tracks	348 (0.8%)	773 (1.7%)
No count in one or more planes	7	15

Table 4

Reconstruction Efficiency of E12 M Trigger

<u>Intensity</u>	<u>Rec. Effect of E12 M Triggers</u>
4.0 x 10 ¹¹	86.9%
6.8 x 10 ¹¹	84.7%
8.3 x 10 ¹¹	82.8%
14.0 x 10 ¹¹	81.6%
16.0 x 10 ¹¹	78.0%

Table 5

Long Lived Sources of Electrons

in Units of π^0 Dalitz Decay Electrons

$K^+ \rightarrow \pi^0 e^+ \nu$	2×10^{-2}
$K_L^0 \rightarrow \pi e \nu$	13×10^{-2}
$K^- \rightarrow \pi e^- \nu$	7×10^{-3}
Hyperons	$< 10^{-3}$
$K_S^0 \rightarrow \pi^0 \pi^0$	2×10^{-2}
$\mu \rightarrow e \nu \nu$	2×10^{-5}
$\pi \rightarrow e \nu$	1×10^{-3}

Table 6

Short Lived Sources of Electrons

In Units of π^0 Dalitz Decay Electrons

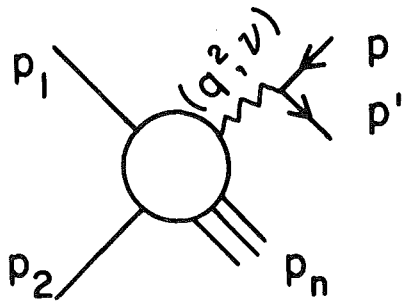
$\pi^0 \rightarrow \gamma\gamma \rightarrow e^+e^-$	1.3 per 1% radiation length
$\pi^0 \rightarrow \gamma e^+ e^-$	1.0
$\eta^0 \rightarrow \gamma e^+ e^-$	0.15 (η^0/π^0) is left after extrapolation to zero matter
$\rho \rightarrow e^+ e^-$	0.03 (ρ/π)
$\omega \rightarrow e^+ e^-$	0.05 (ω/π)
$\phi \rightarrow e^+ e^-$	0.2 (ϕ/π)
Signal	~ 1.2 at $\theta = 50$ mrad ~ 0.6 at $\theta = 83$ mrad

FIGURE CAPTIONS

- Fig. 1 Graph for deep inelastic lepton nucleon scattering
- Fig. 2 Graph for lepton pair production in hadron-hadron collisions
- Fig. 3 Schematic diagram of the spectrometer
- Fig. 4 Geometric arrangement of the lead glass calorimeter
- Fig. 5 The acceptance of the spectrometer for a typical spectrometer setting ($\theta_{\text{LAB}} = 50 \text{ mr}$, $I = 700 \text{ A}$ and 1000 A)
- Fig. 6 The trigger logic
- Fig. 7 E/P distribution with and without longitudinal shower development cuts
- Fig. 8 E/P distributions with and without E, EP cuts
- Fig. 9 Electron yield as a function of converter thickness
0.7% data point corresponds to target plus miscellaneous matter but no converter
- Fig. 10 The ratio of directly produced electrons and electrons from photon conversion as function of P_{T} at 50 mr
- Fig. 11 Same as Fig. 10 but at 83 mr
- Fig. 12 The charge asymmetry of directly produced electrons at 50 and 83 mr
- Fig. 13 The invariant cross section of directly produced electrons as function of P_{T} , averaged over both signs at $\theta = 50$ and 83 mrad
- Fig. 14 The invariant cross section of conversion electrons as a function of P_{T} , averaged over both signs at

- Fig. 14
cont'd $\theta = 50$ and 83
- Fig. 15 The trigger efficiencies of E12L, E12M and E12H as a function of P_T . Shower cuts (cut 1) are applied, $\theta = 83 \pm 400$ A corresponds to lowest energy in the lead glass calorimeter
- Fig. 16 The pulse height of the T_2 trigger counter for hadrons and for electrons are at $\theta = 50$ mr
 $I = 1000$ A
- Fig. 17 Reconstruction efficiency after the addition of a random trigger as function of P_T
- Fig. 18 Efficiency of the longitudinal shower development cut (cut 1) as function of P_T at $\theta = 50$ mr and 83 mr
- Fig. 19 E/P distributions with different cuts on the lateral spread of the shower
- Fig. 20 Consistency of the two analyses using cuts type 1 and 2 respectively
- Fig. 21 Average fractional energy deposition in a block of lead glass as a function of the position of a track
- Fig. 22 A histogram of the number of events that deposit a given relative fraction of their energy outside the standard shower core
- Fig. 23 E/P histograms with 1, 2 or 3 πe firing along a track. Shower cut type 1 is applied

- Fig. 24 The cross section for single lepton production in pp collisions using a parton model (curve γ_V). W^+ or B^0 bumps rise from this up to the curves labelled W and B^0 , respectively
- Fig. 25 A speculation about a new lepton-X-parton interaction
- Fig. 26 Arrangement of the strips of scintillation of the hodoscopes. Note the overlap
- Fig. 27 A fit of the analytic shower theory to a Monte Carlo result
- Fig. 28 The spectrum of π^0 whose γ 's are incident on a 5.1 cm thick lead filter and the spectrum of electrons (of one charge) that exit from the filter
- Fig. 29 The number of electrons of one charge that exit from a filter as function of the filters thickness
- Fig. 30 The 2 body decay suppression in the process $\pi^0 \rightarrow \gamma\gamma$



LEPTON PAIR PRODUCTION

FIG. 1

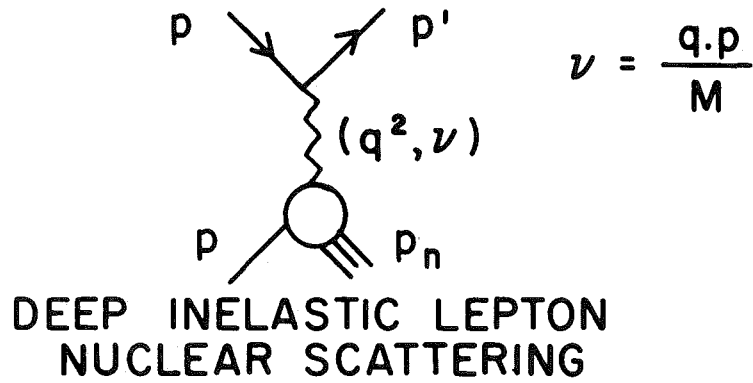


FIG. 2

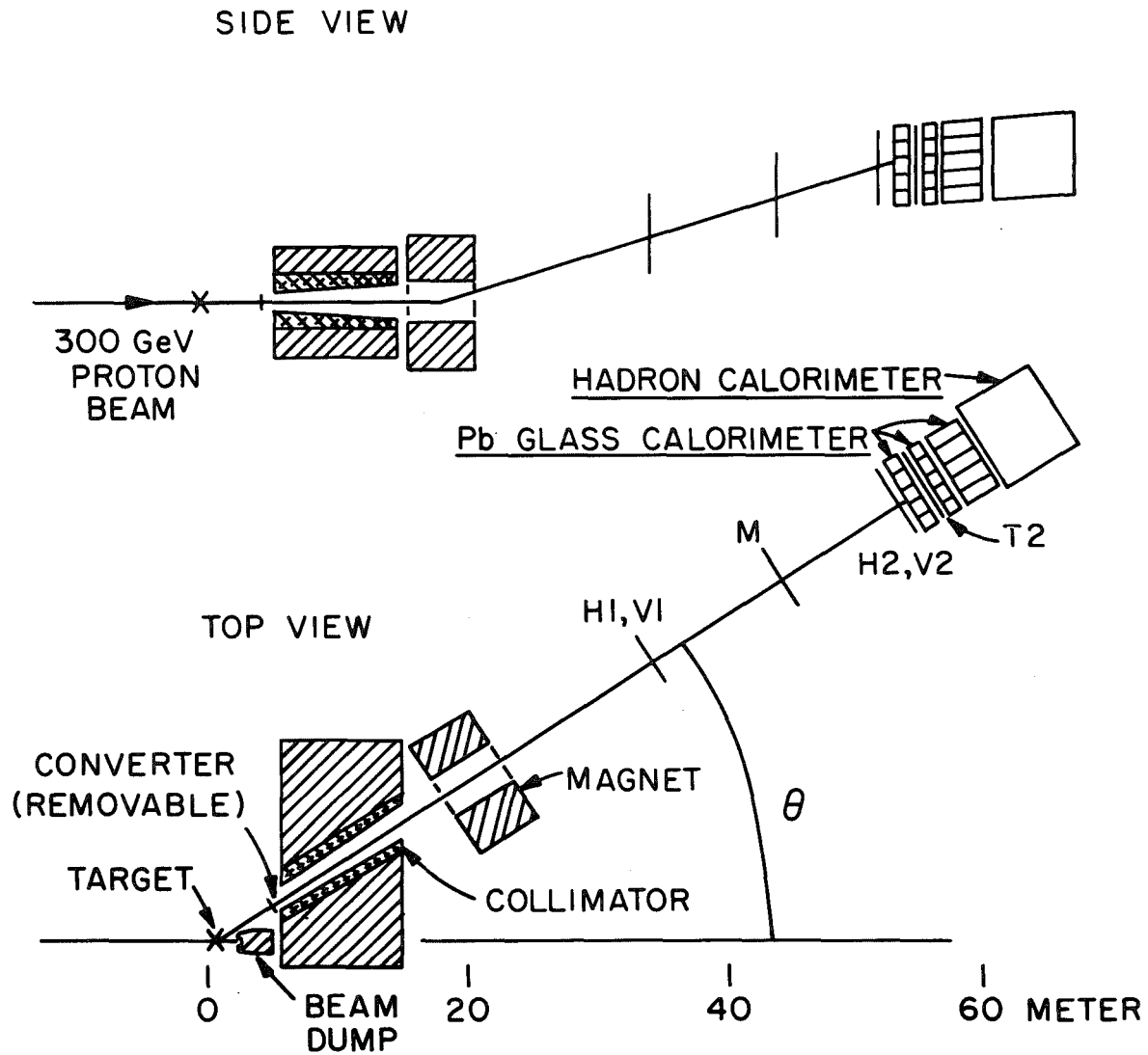


FIG. 3

LEAD GLASS CALORIMETER

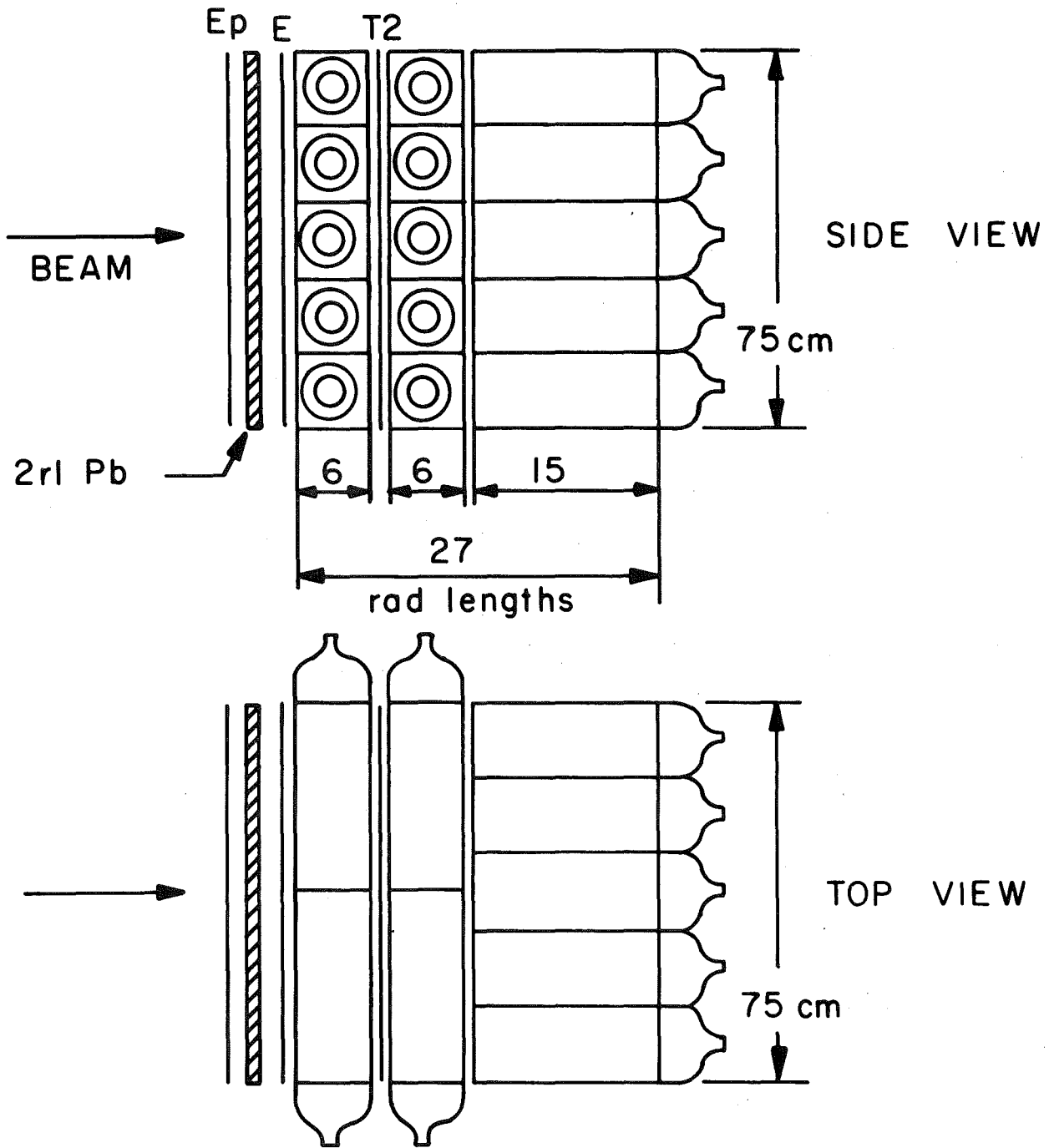


FIG. 4

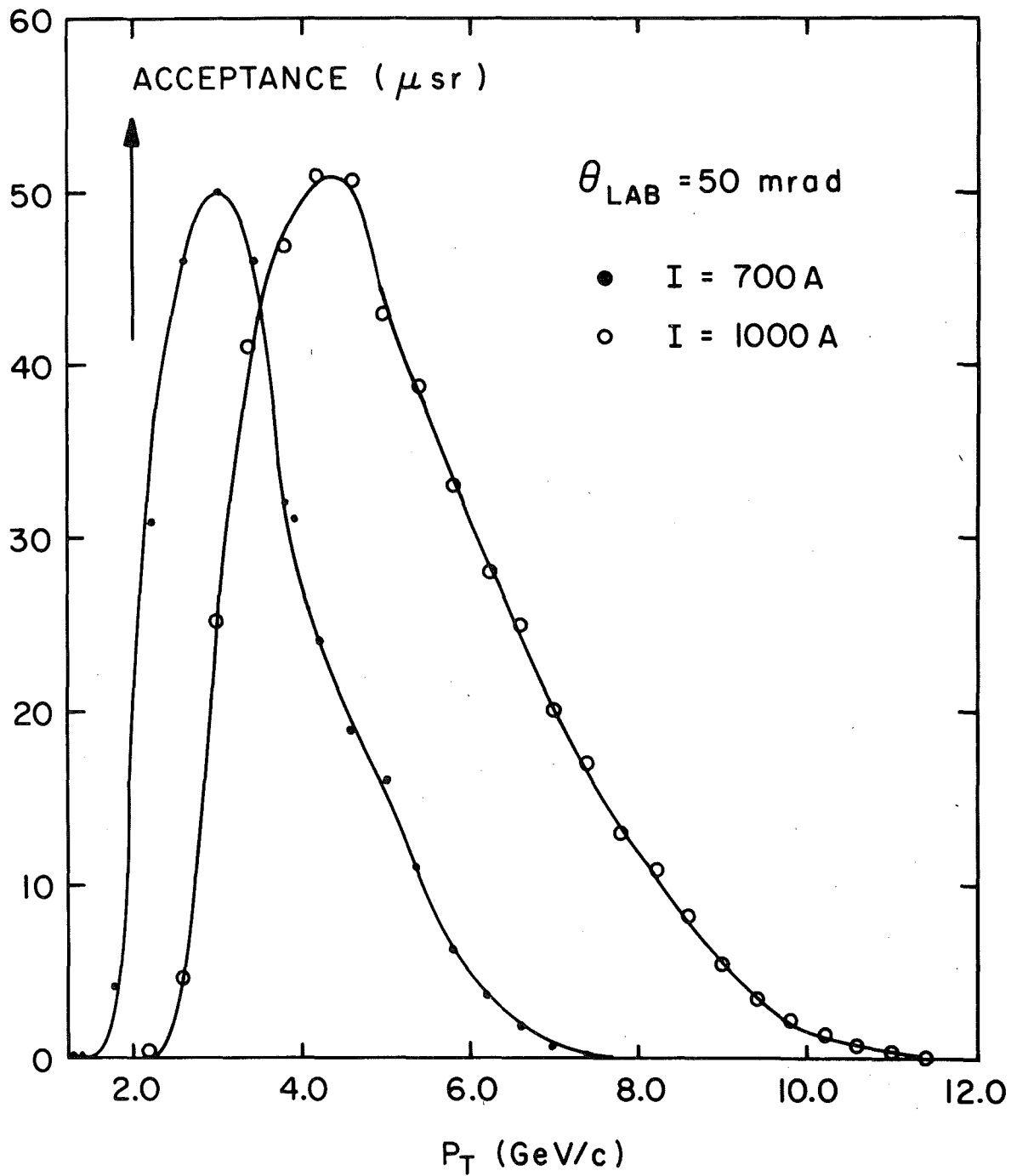


FIG. 5

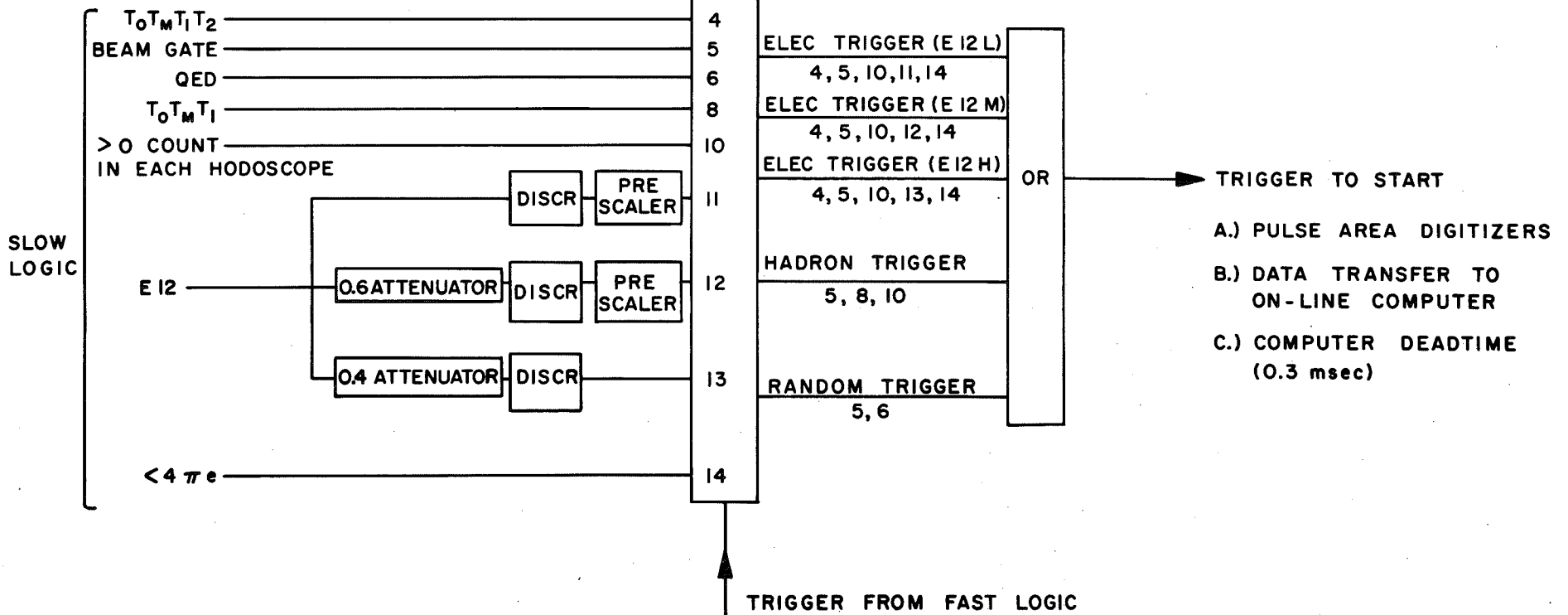
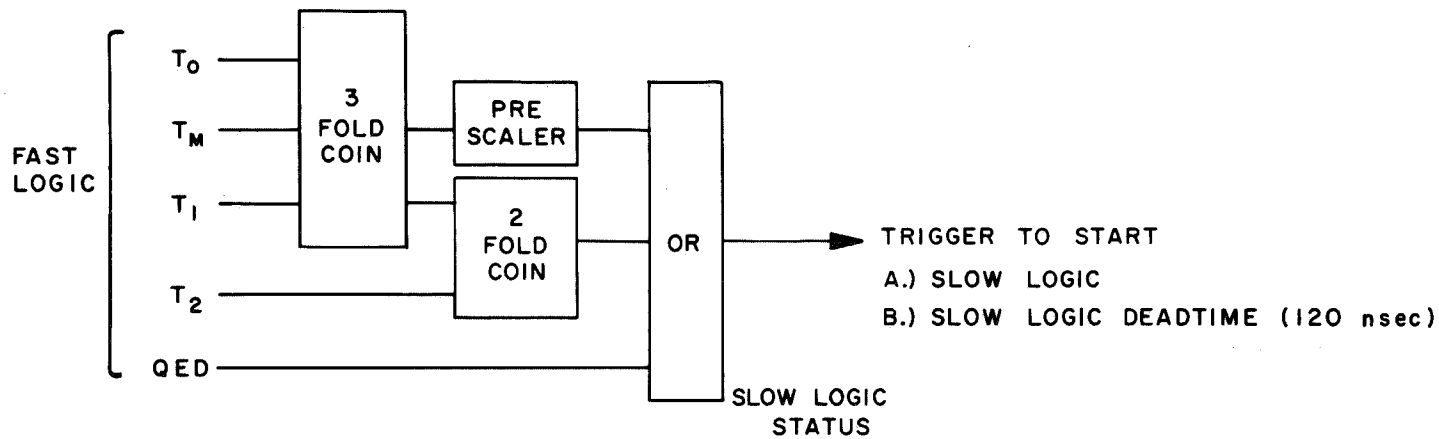


FIG. 6

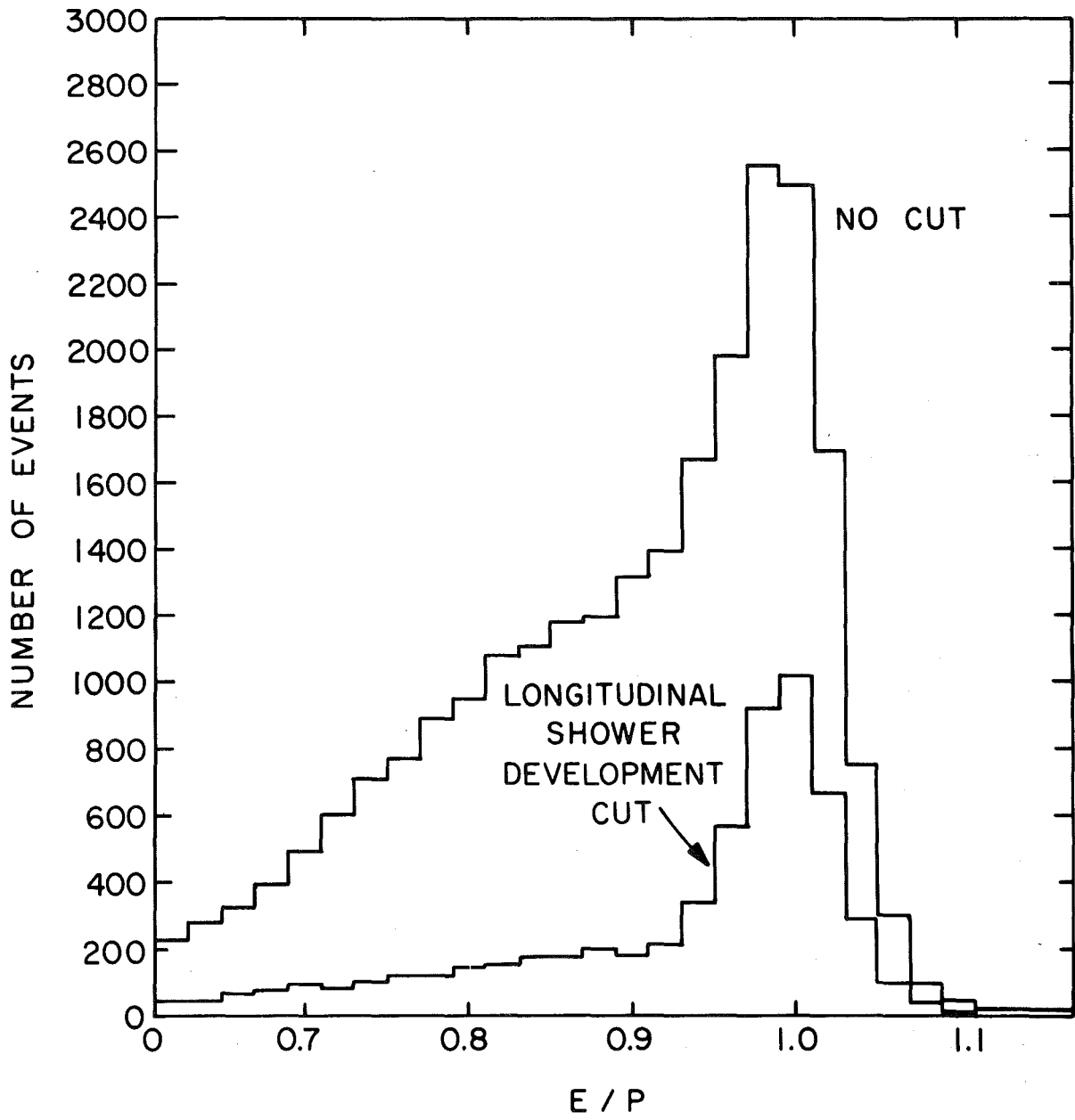


FIG. 7

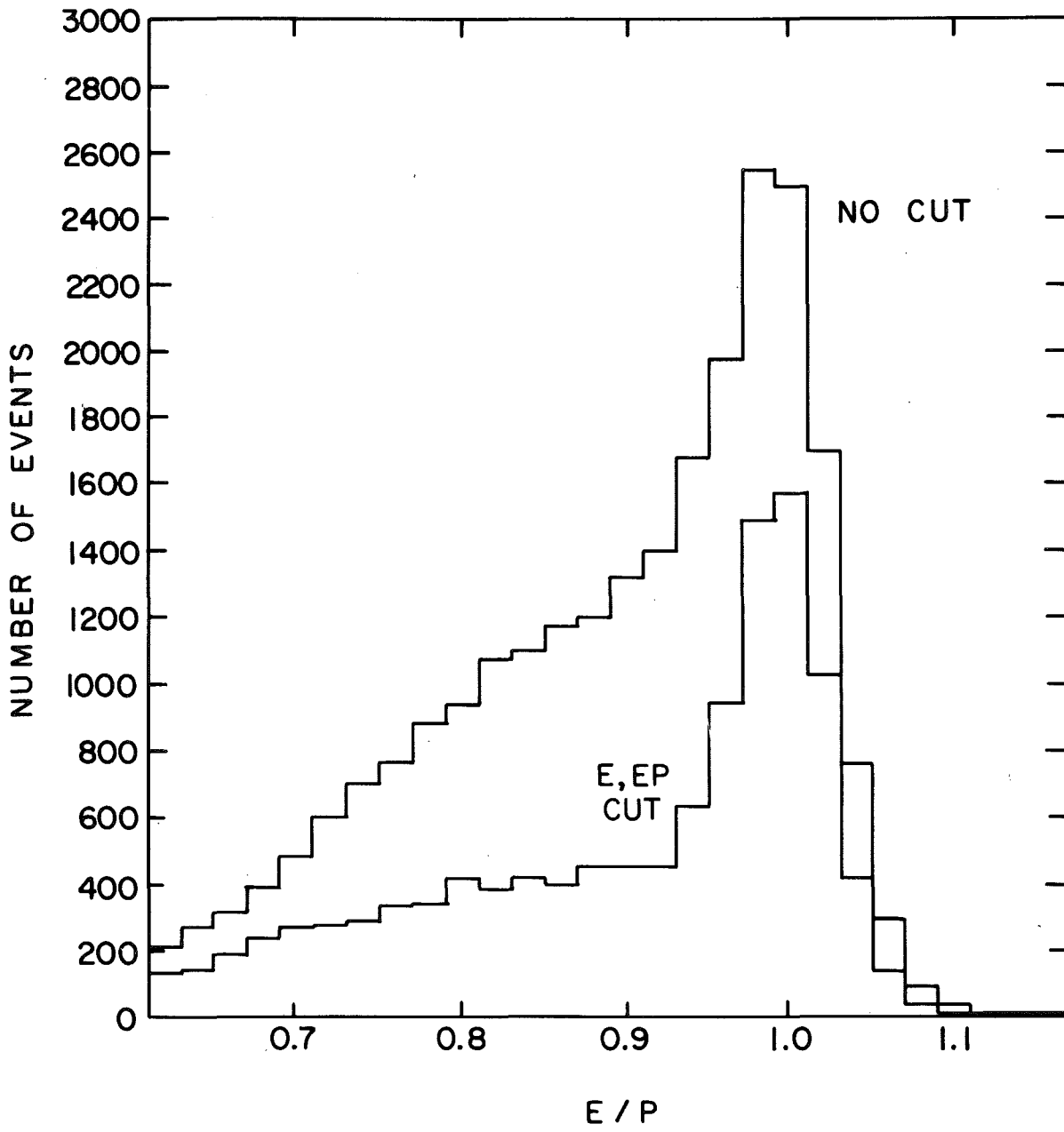


FIG. 8

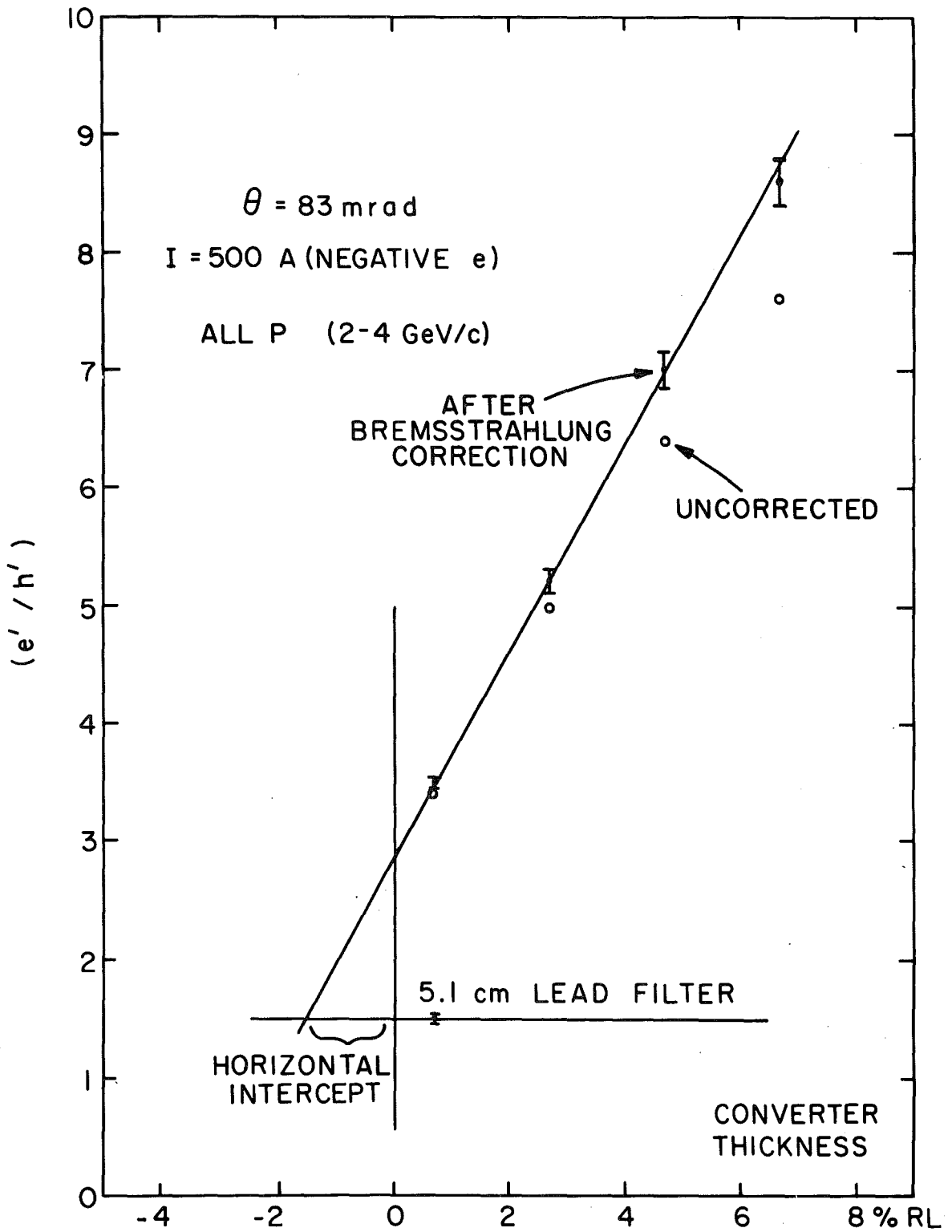


FIG. 9

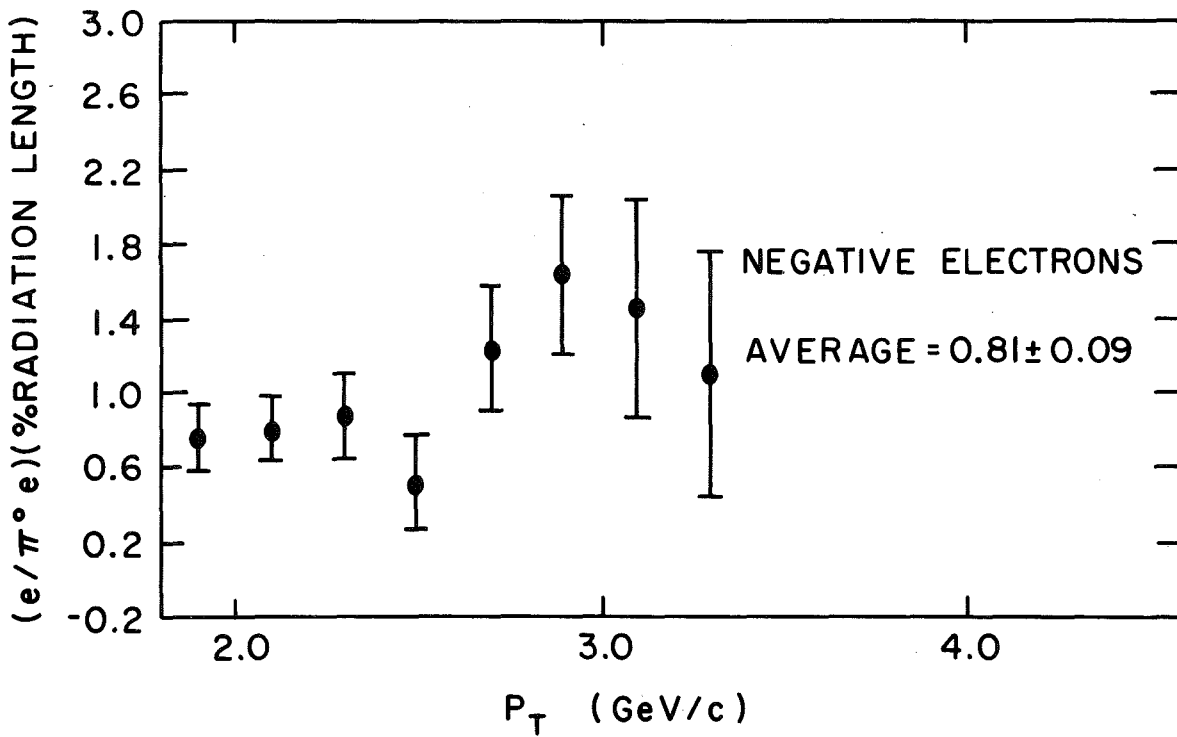
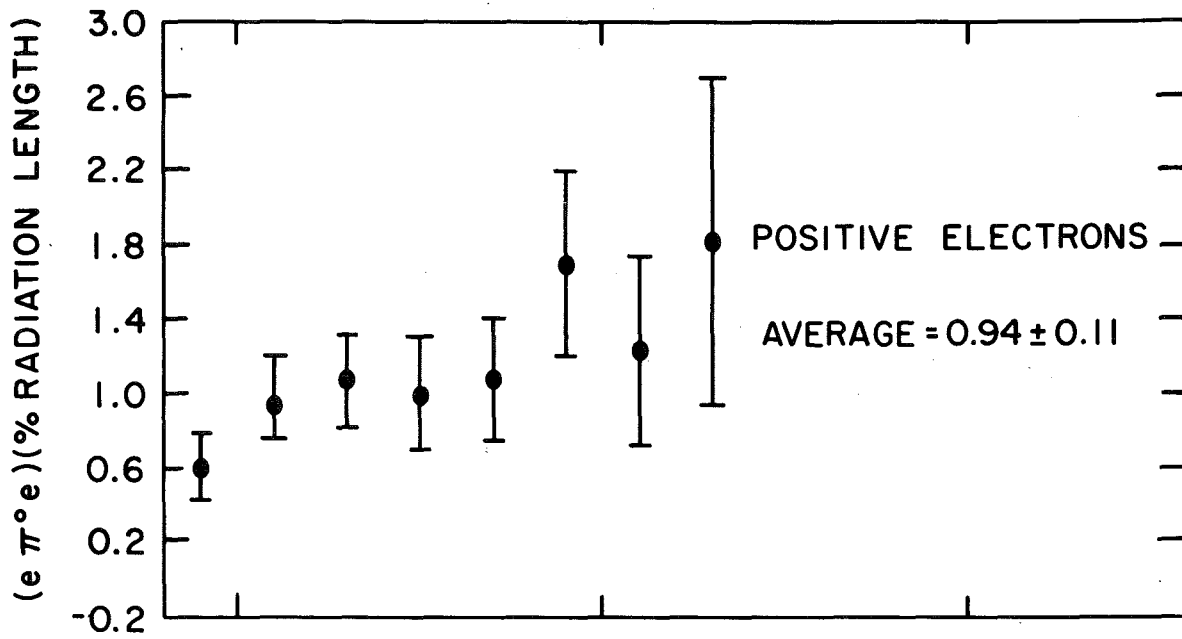


FIG. 10

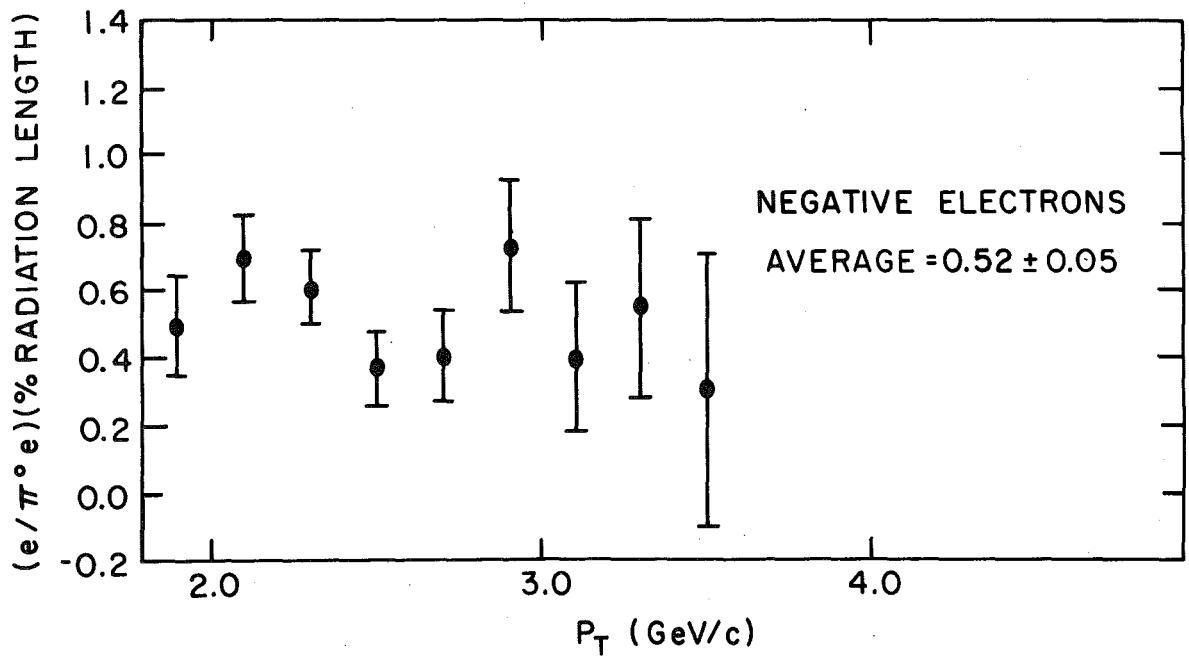
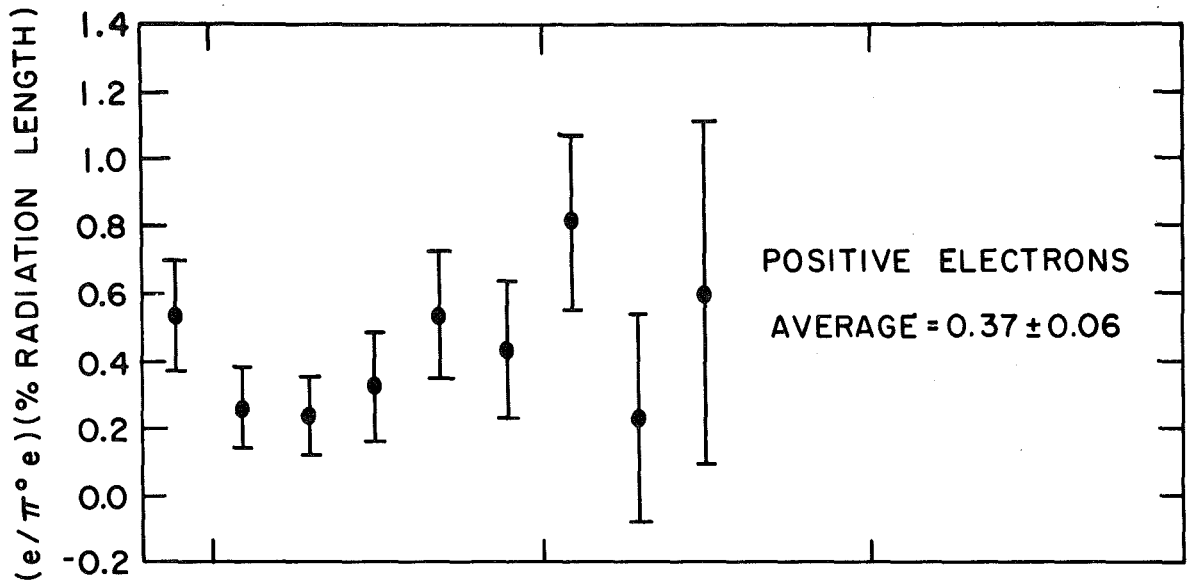


FIG. II

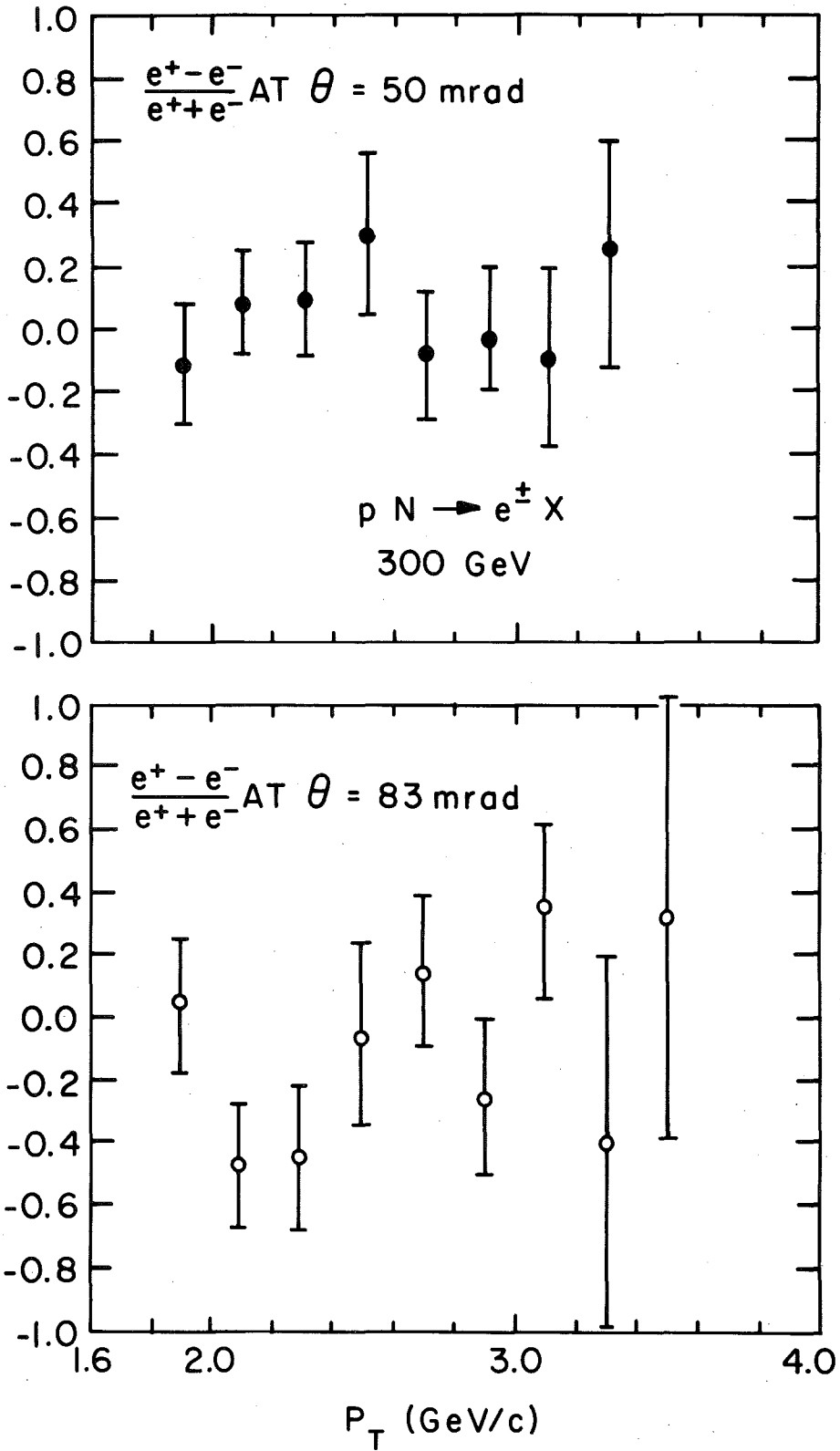


FIG. 12

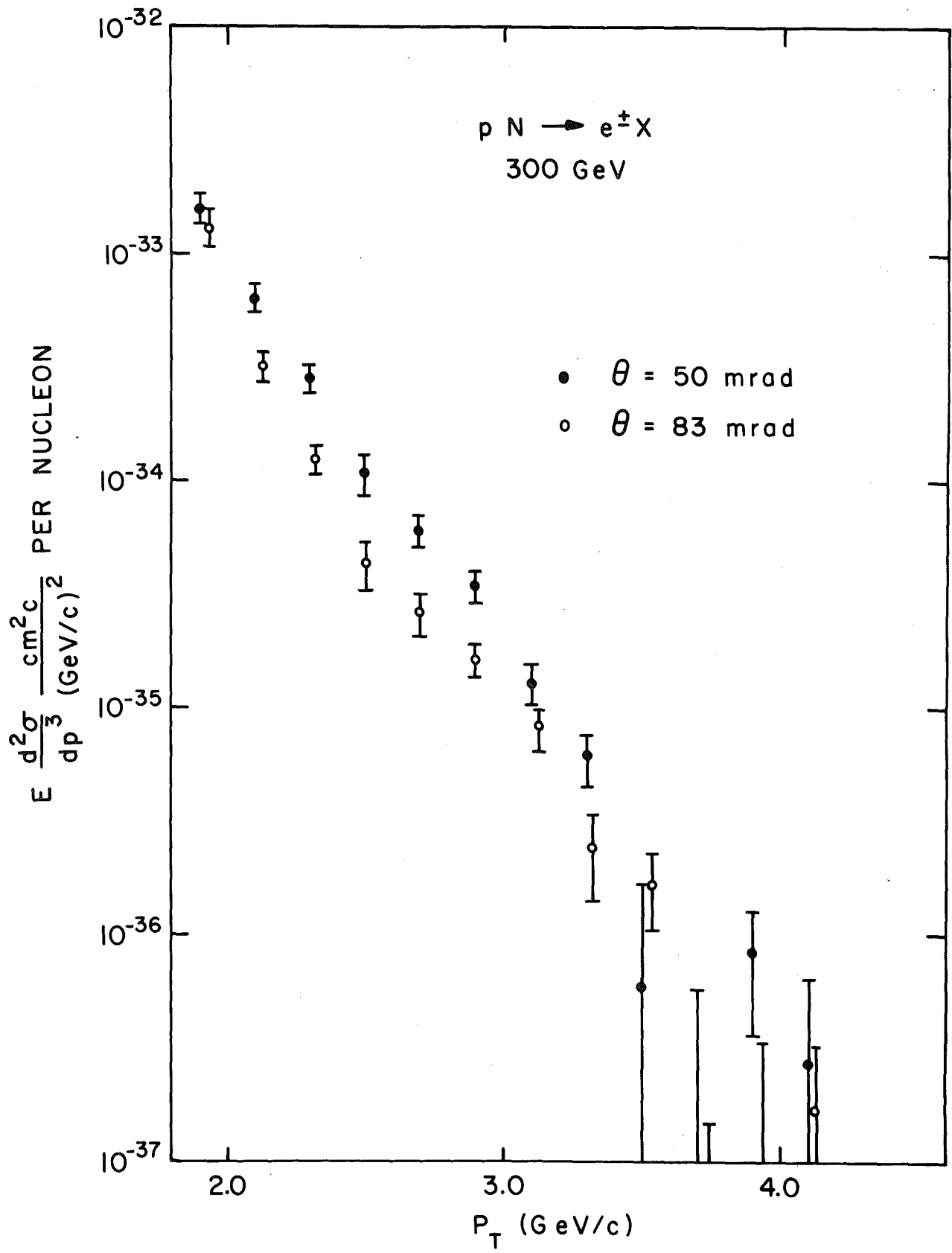


FIG. 13

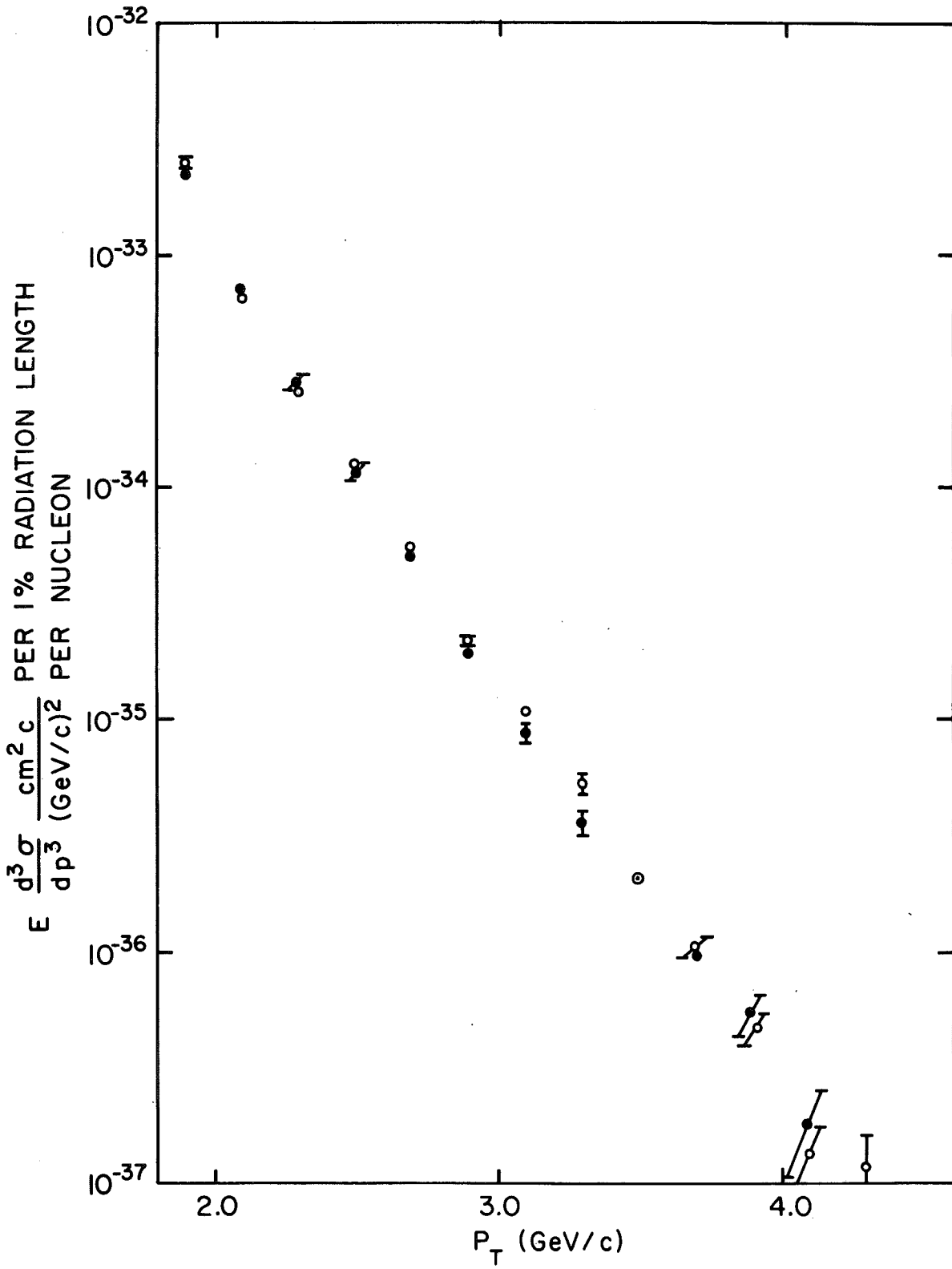


FIG. 14

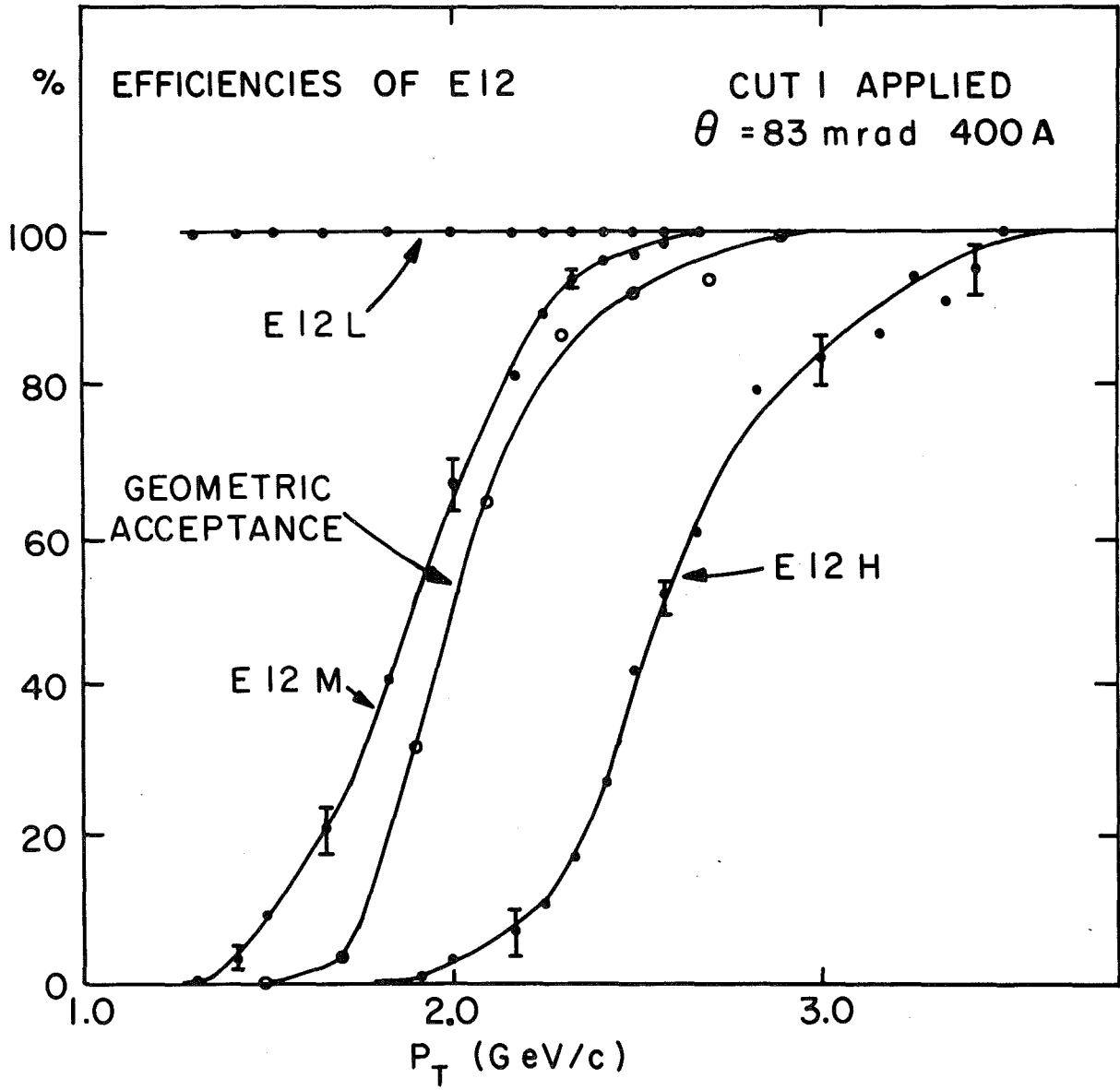


FIG. 15

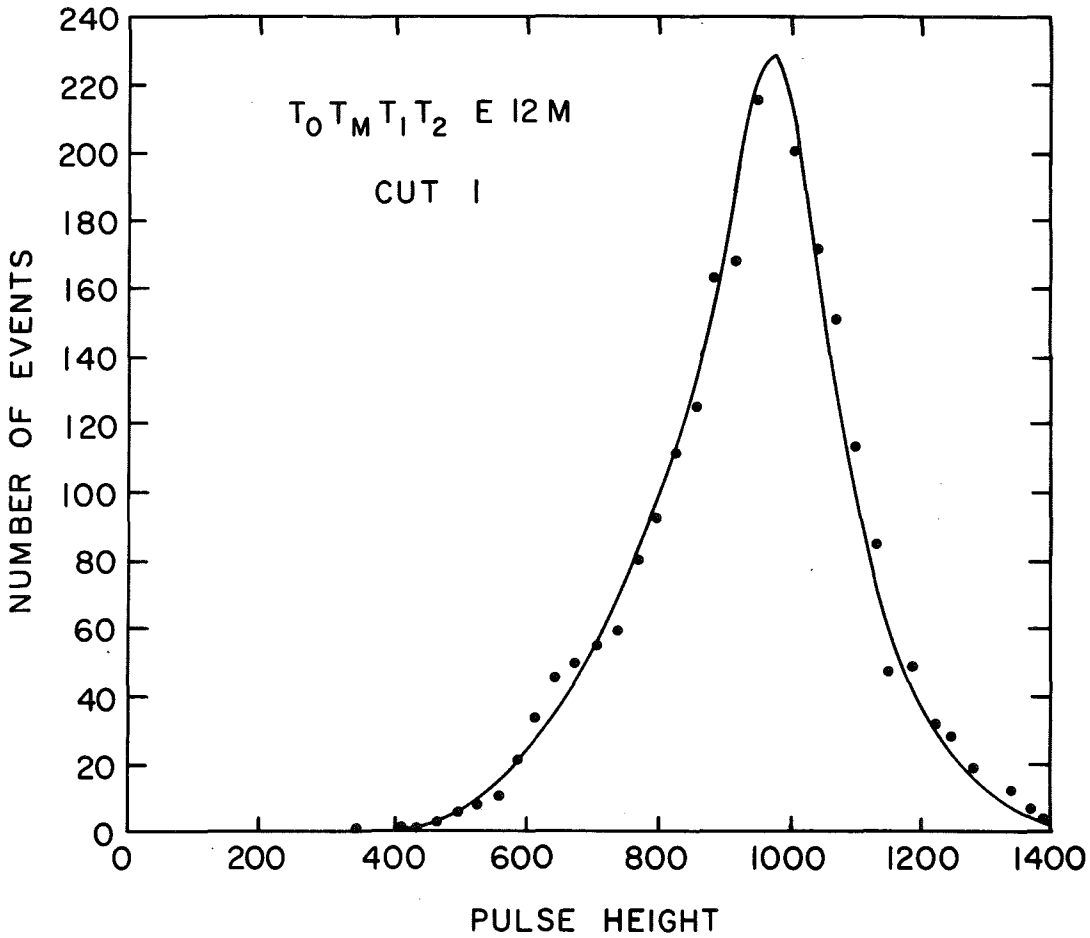
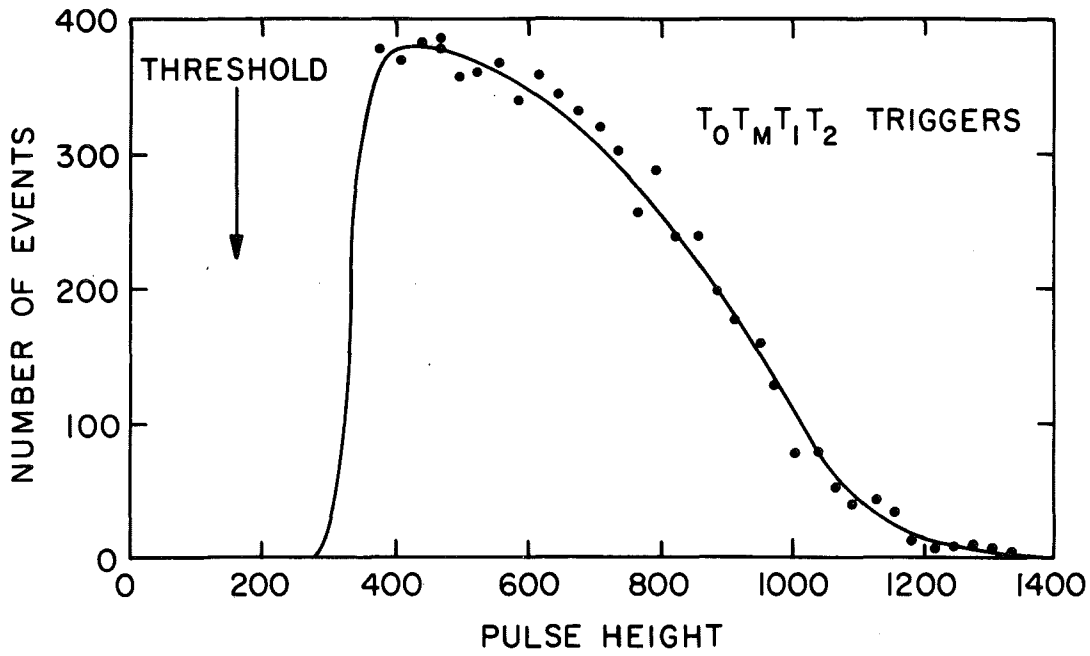


FIG. 16

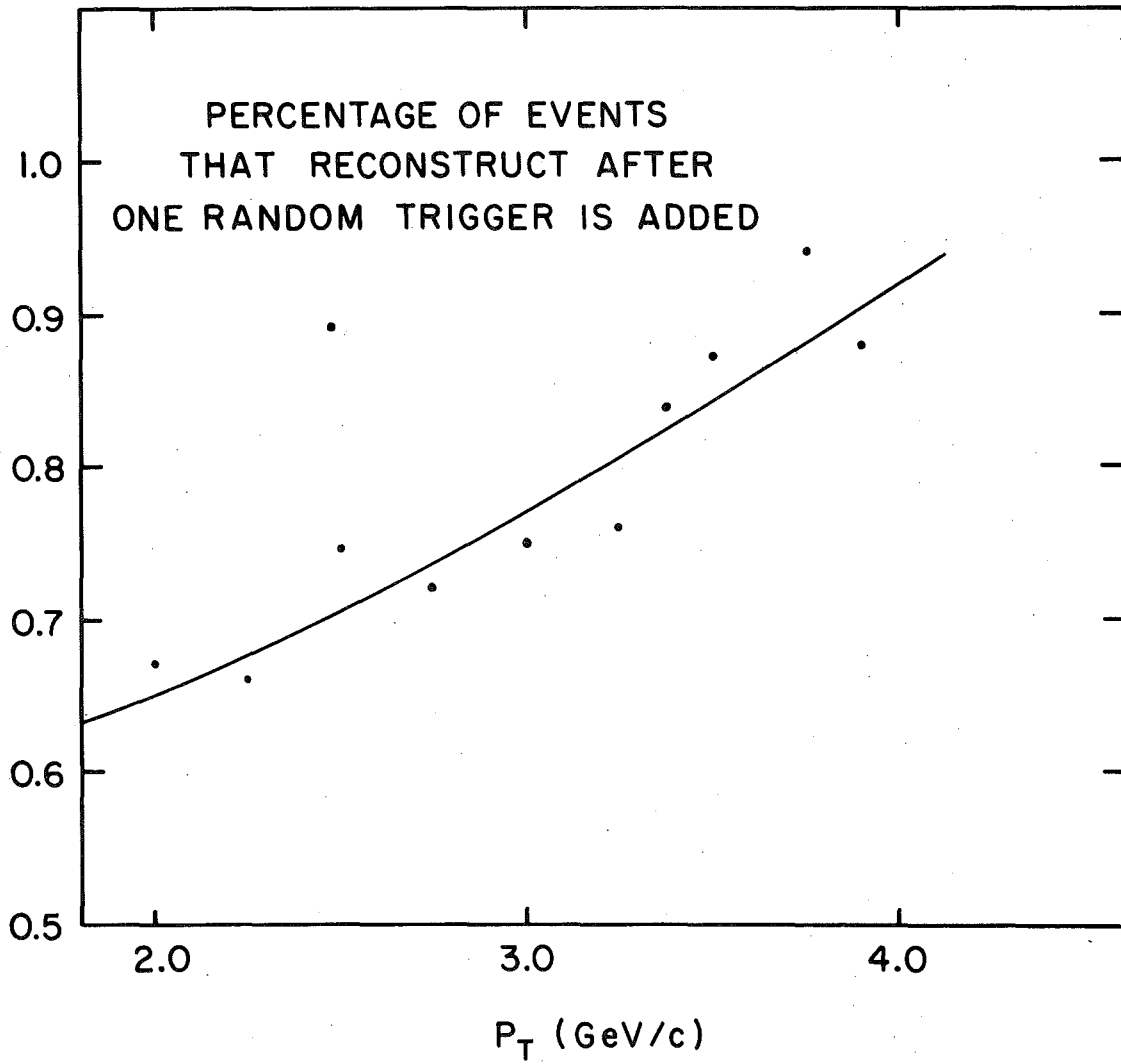


FIG.17

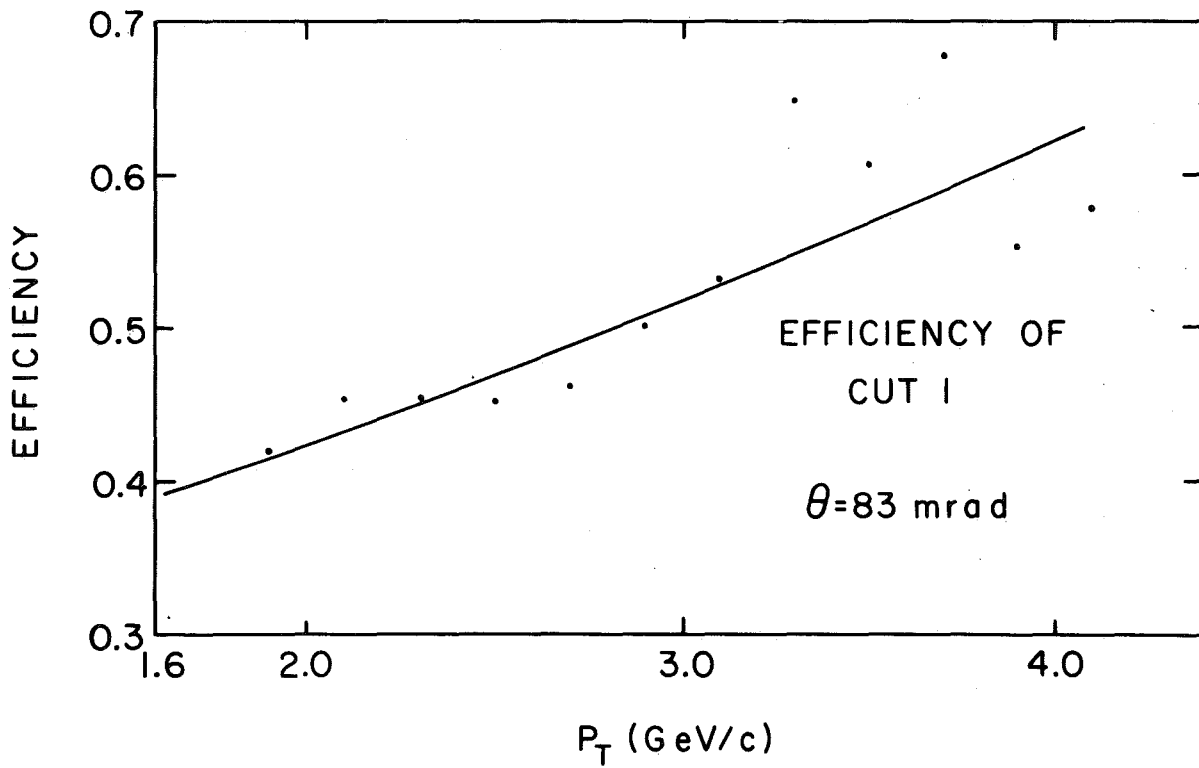
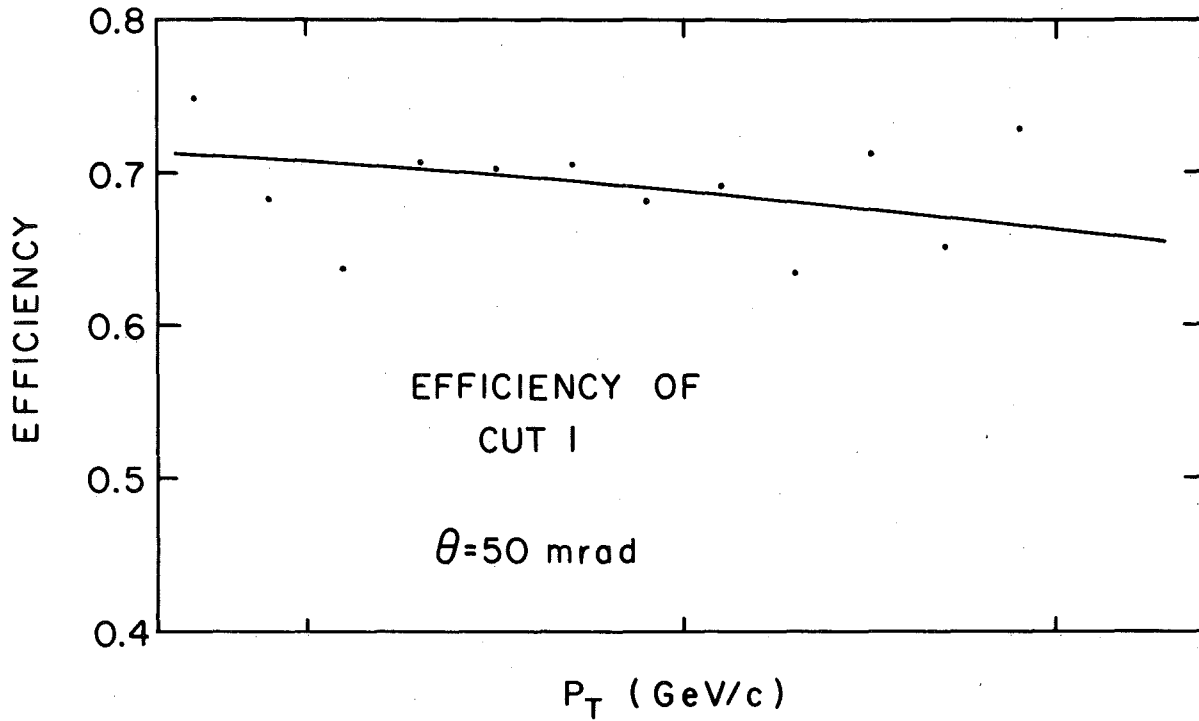


FIG. 18

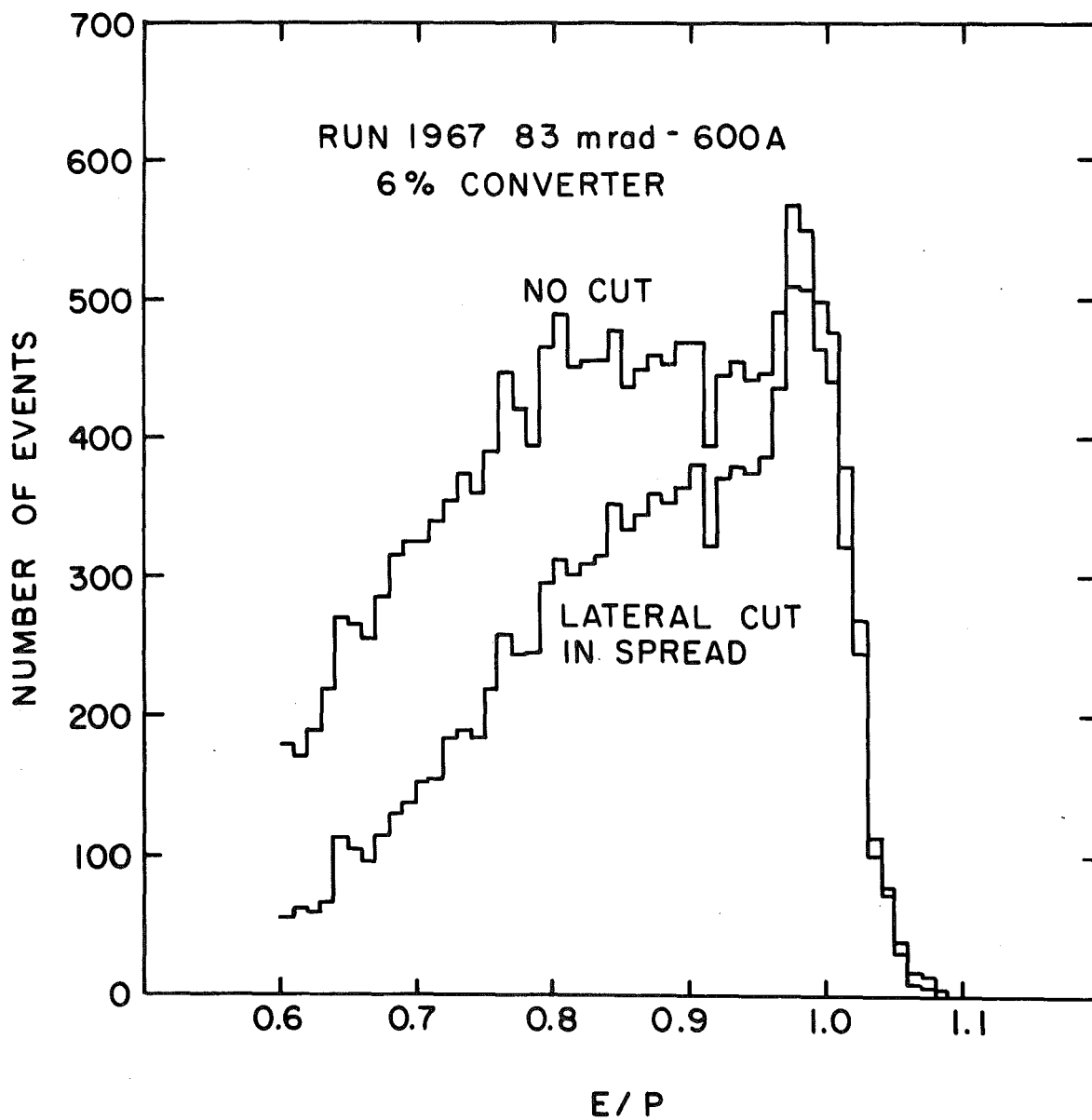


FIG. 19

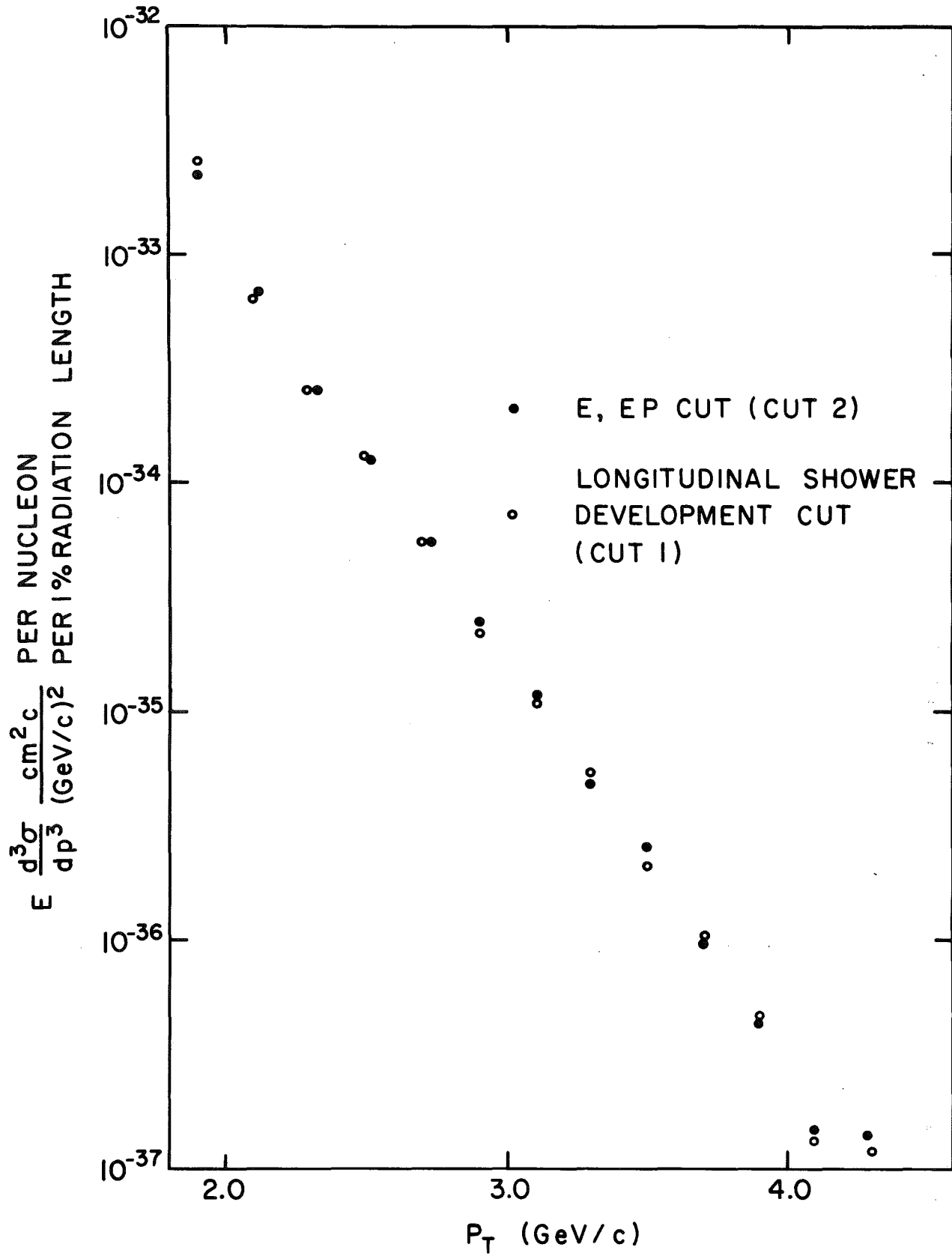


FIG. 20

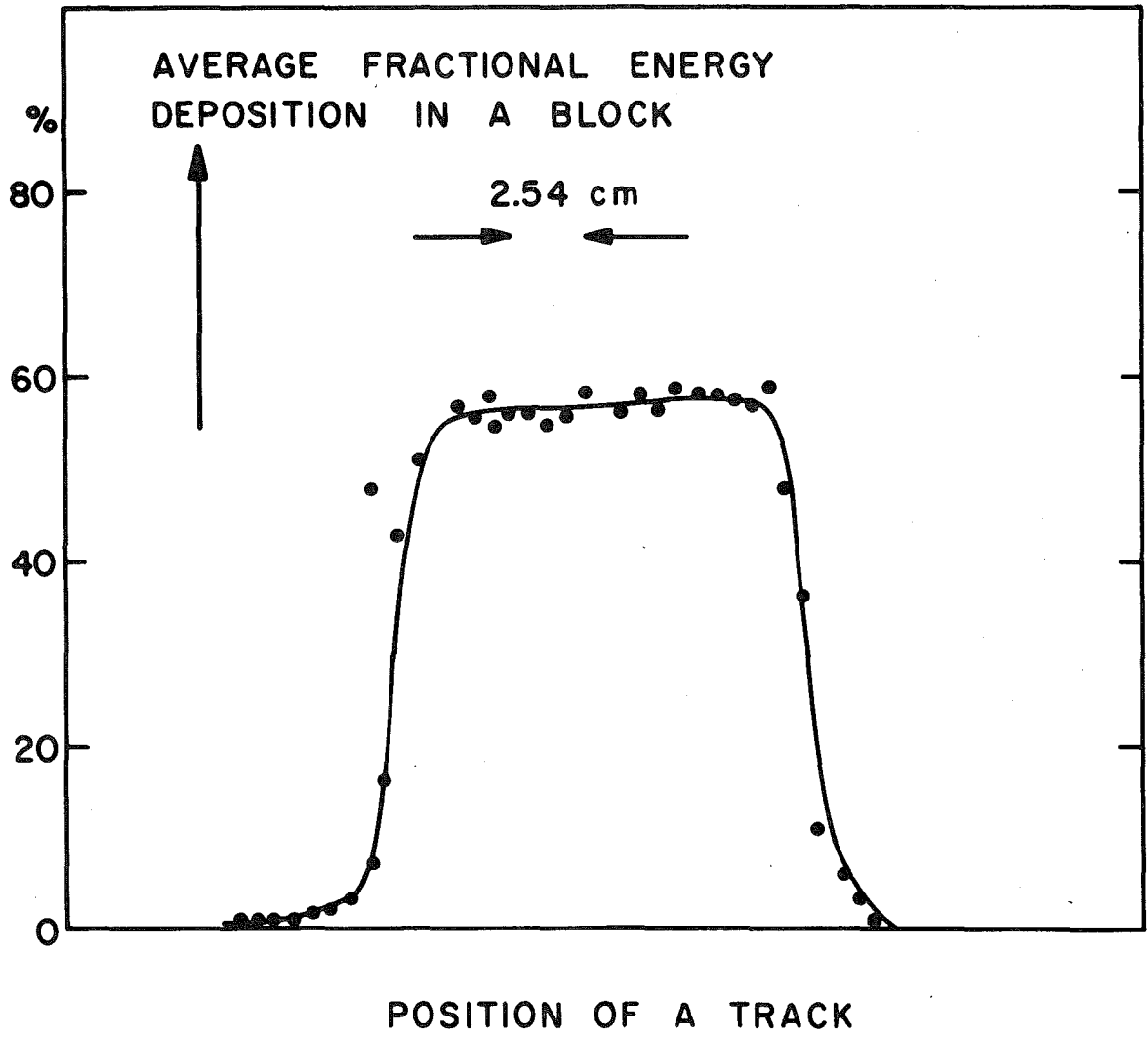


FIG. 21

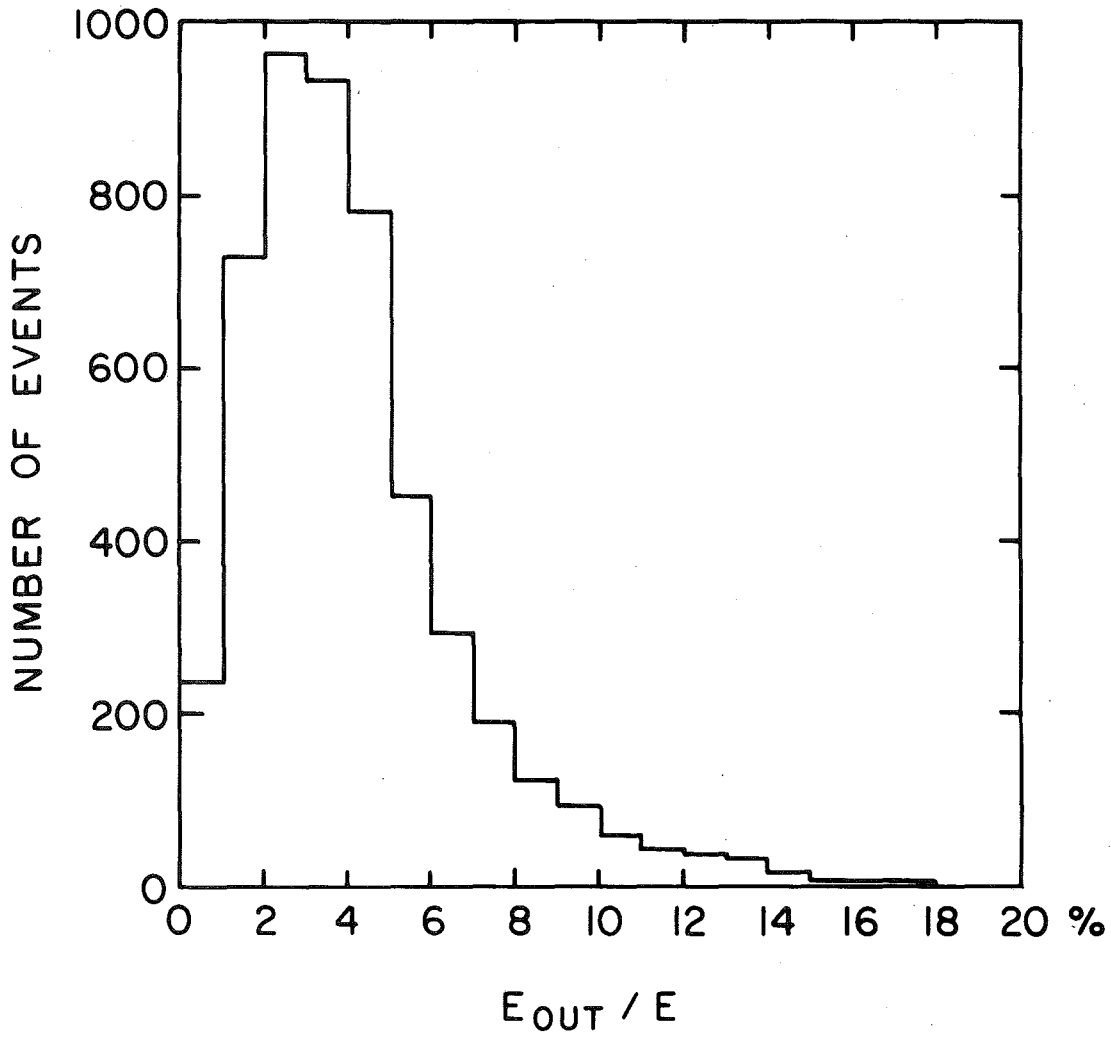


FIG. 22

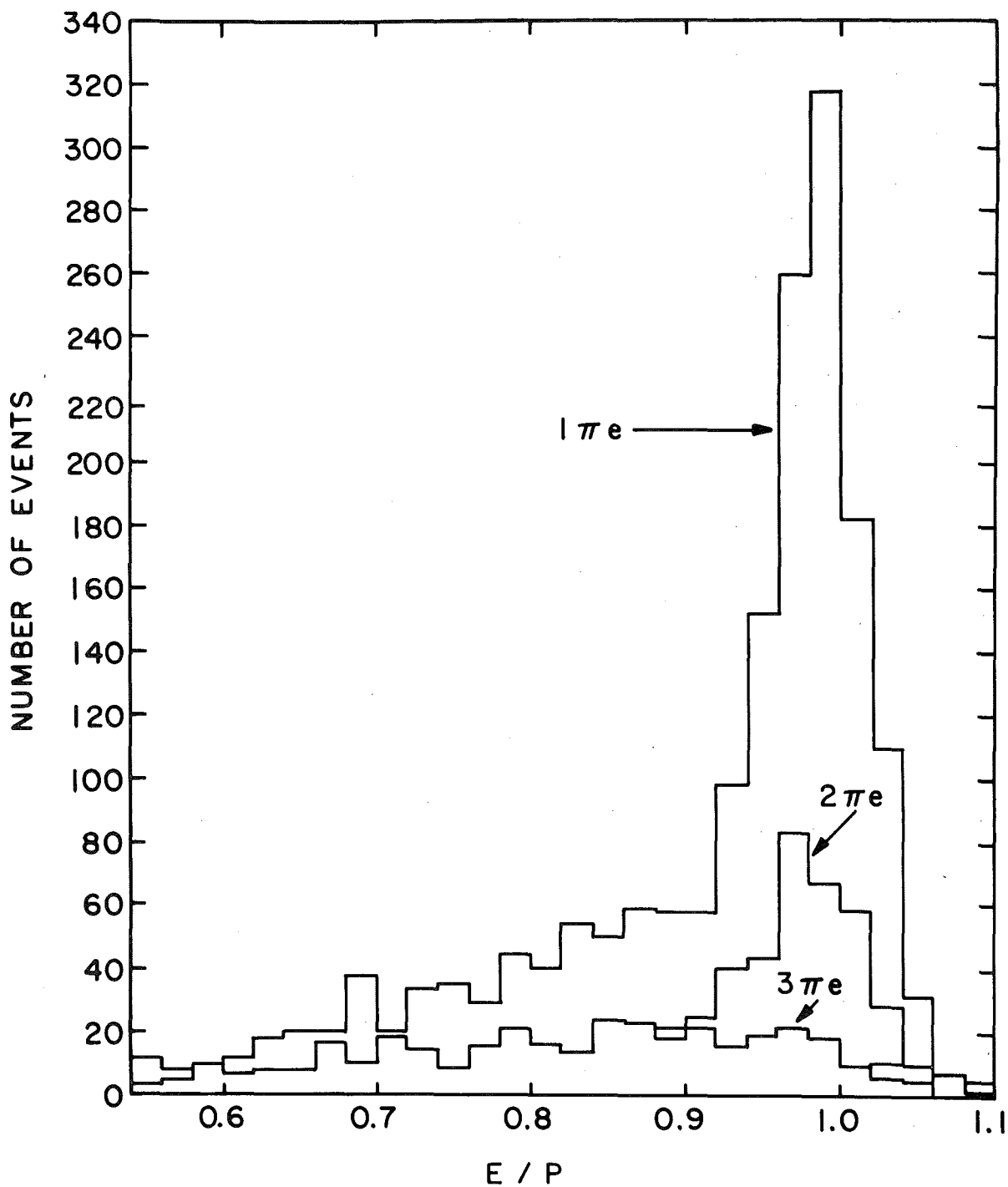


FIG. 23

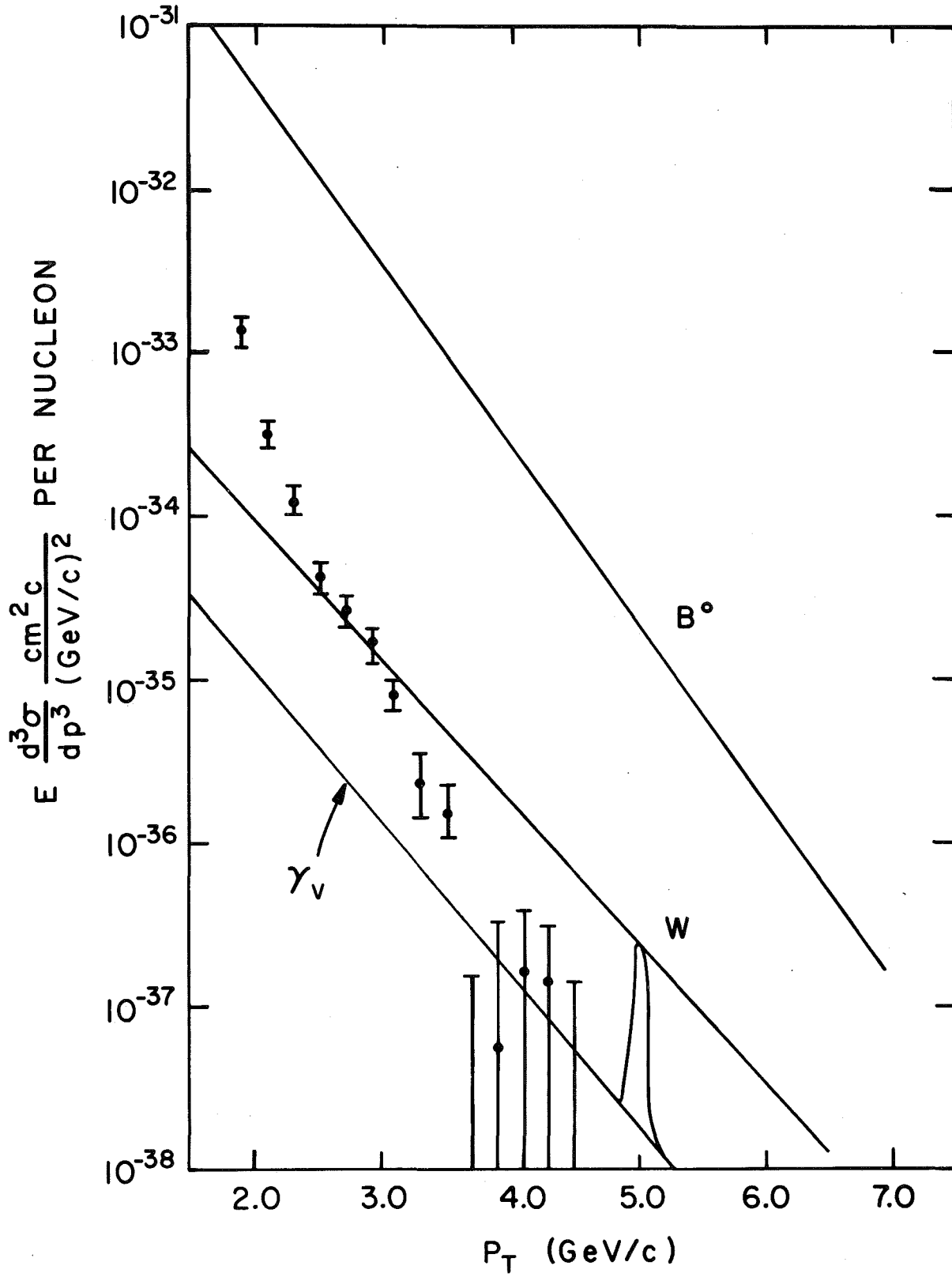


FIG. 24

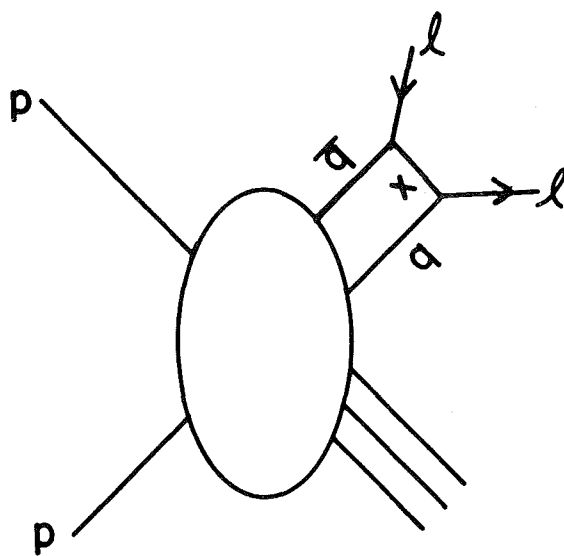


FIG. 25

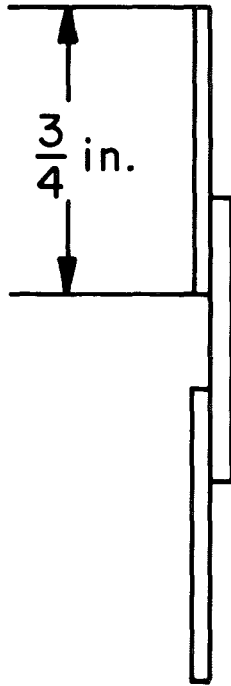


FIG. 26

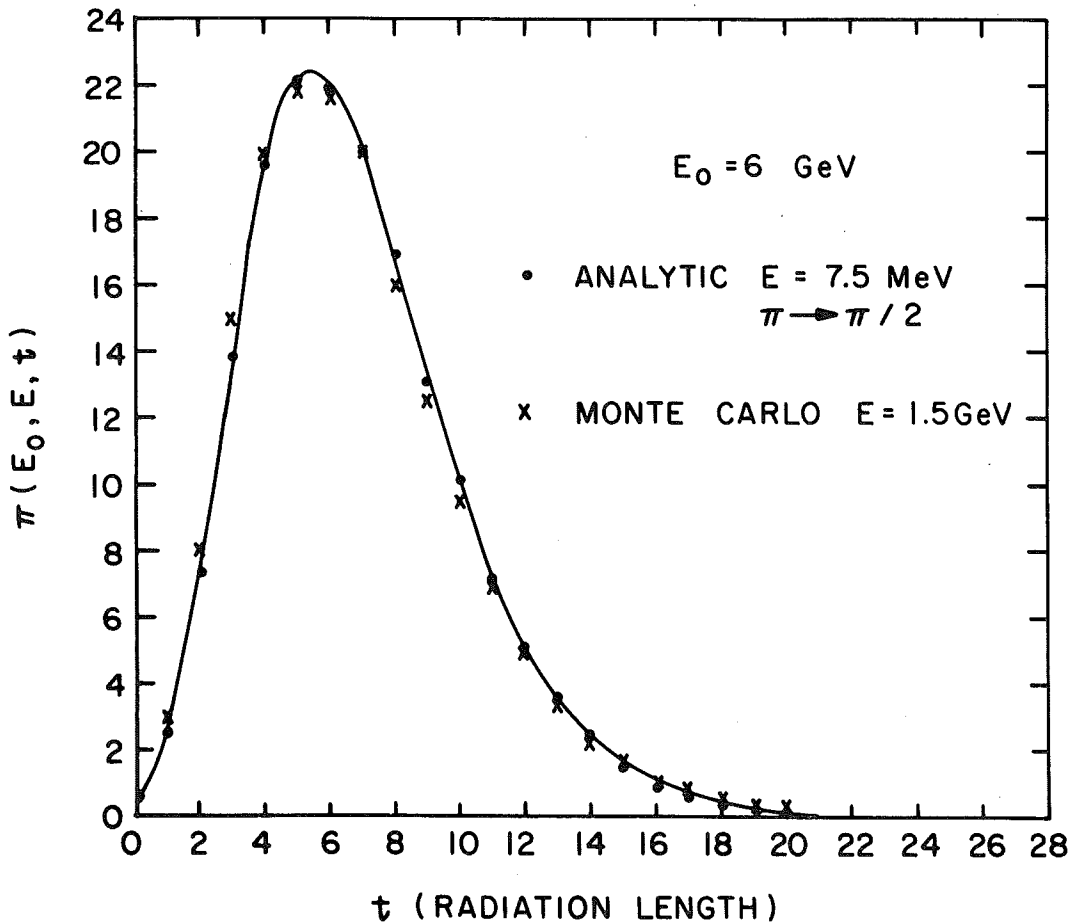
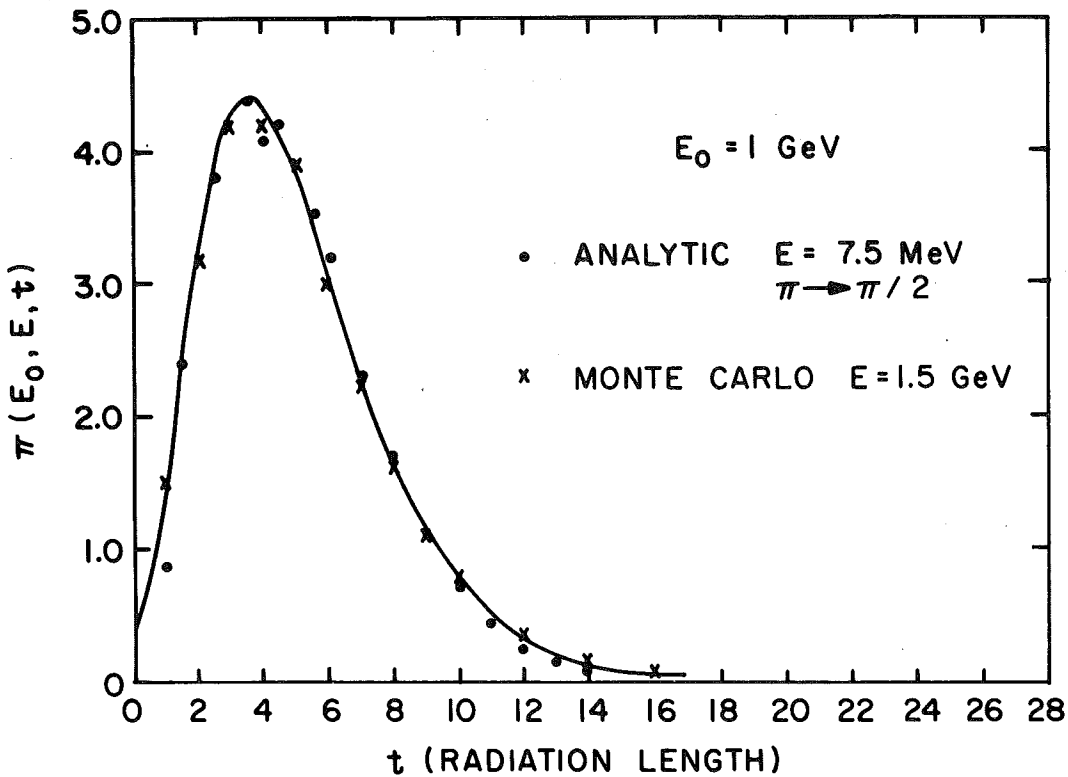


FIG. 27

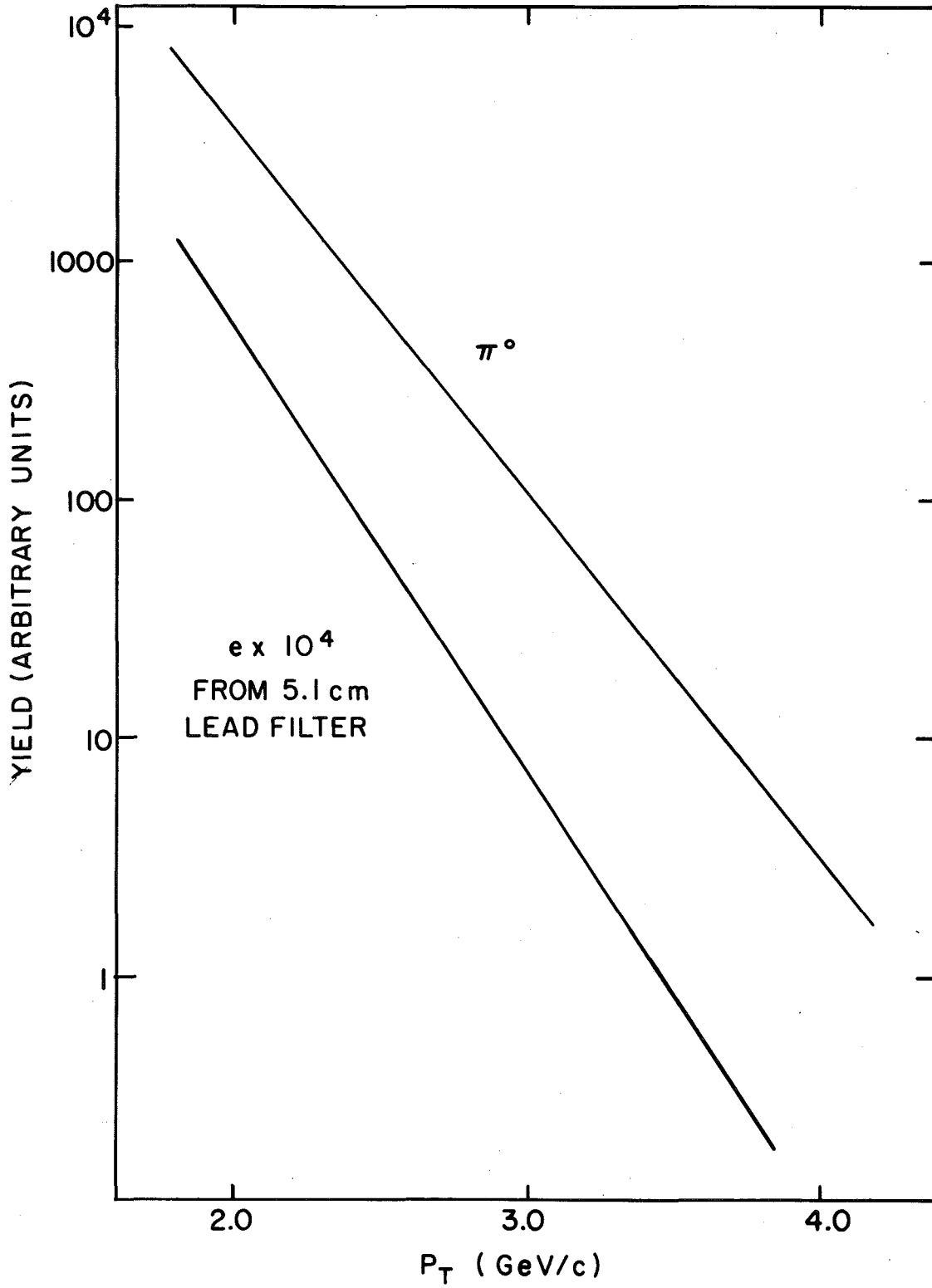


FIG. 28

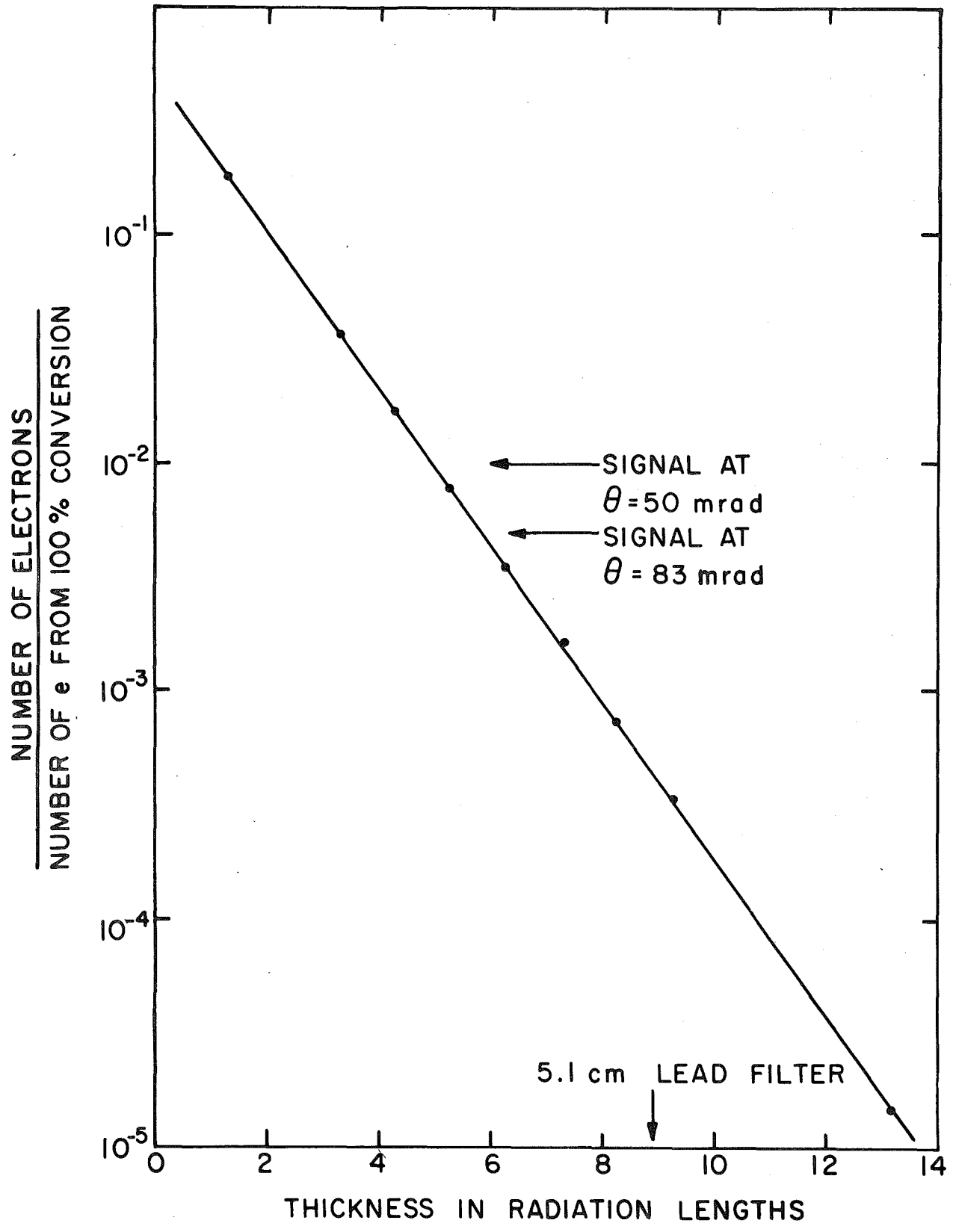


FIG. 29

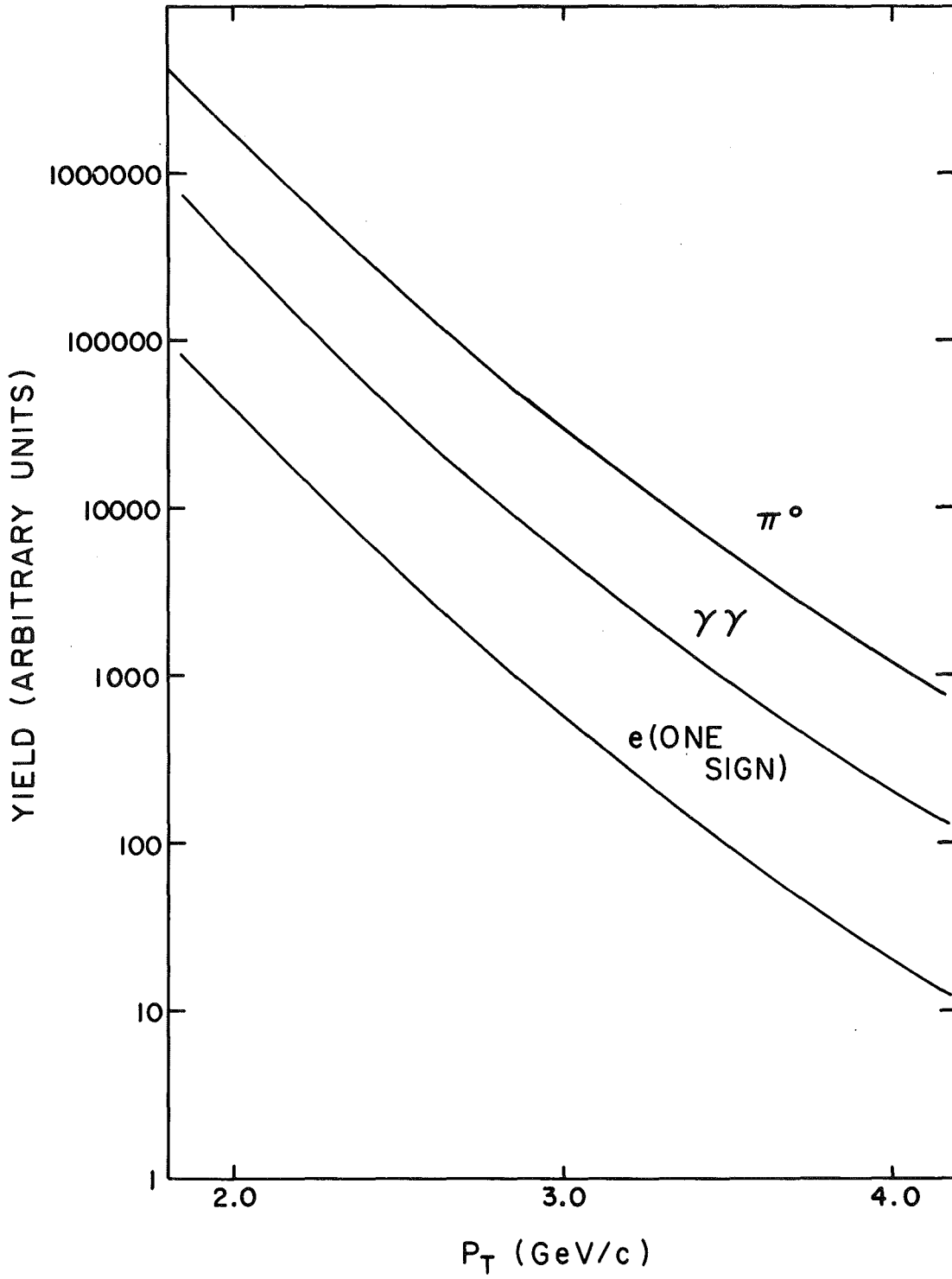


FIG. 30